Glymphatic-assisted perivascular brain delivery of intrathecal small gold nanoparticles

Lilius, Tuomas O.; Mortensen, Kristian Nygaard; Deville, Claire; Lohela, Terhi J.; Stæger, Frederik Filip; Sigurdsson, Björn; Rosenholm, Marko; Beekman, Freek J.; Jensen, Andreas I.; More Authors

Important note
To cite this publication, please use the final published version (if applicable).
Please check the document version above.

Glymphatic-assisted perivascular brain delivery of intrathecal small gold nanoparticles

Tuomas O. Lilius [a,b,c,d,1], Kristian Nygaard Mortensen [a,1], Claire Deville [e], Terhi J. Lohela [a,c,f], Frederik Filip Stæger [a], Björn Sigurdsson [a], Elisabetta M. Fiordaliso [g], Marko Rosenholm [a,c], Chris Kamphuis [h,1], Freek J. Beekman [h,i,j], Andreas I. Jensen [e,2,**], Maiken Nedergaard [a,k,*,2]

[a] Center for Translational Neuromedicine, Faculty of Health and Medical Sciences, University of Copenhagen, Copenhagen, Denmark
[b] Department of Pharmacology, Faculty of Medicine, University of Helsinki, Helsinki, Finland
[c] Individualized Drug Therapy Research Program, Faculty of Medicine, University of Helsinki, Helsinki, Finland
[d] Department of Emergency Medicine and Services, University of Helsinki and Helsinki University Hospital, Finland
[e] The Hevesy Laboratory, Department of Health Technology, Technical University of Denmark, Roskilde, Denmark
[f] Department of Anaesthesiology, Intensive Care Medicine, and Pain Medicine, University of Helsinki and Helsinki University Hospital, Finland
[g] DTU Nanolab – National Center for Nano Fabrication and Characterization, Technical University of Denmark, Kgs. Lyngby, Denmark
[h] Department of Translational Neuroscience, Brain Center Rudolf Magnus, University Medical Center Utrecht, Utrecht, the Netherlands
[i] MILabs B.V., Utrecht, the Netherlands
[j] Department of Radiation Science and Technology, Delft University of Technology, Delft, the Netherlands
[k] Center for Translational Neuromedicine, University of Rochester Medical Center, Rochester, NY, USA

ARTICLE INFO

ABSTRACT

Nanoparticles are ultrafine particulate matter having considerable potential for treatment of central nervous system (CNS) disorders. Despite their tiny size, the blood-brain barrier (BBB) restricts their access to the CNS. Their direct cerebrospinal fluid (CSF) administration bypasses the BBB endothelium, but still fails to give adequate brain uptake. We present a novel approach for efficient CNS delivery of ^{111}In-radiolabelled gold nanoparticles (AuNPs; 10–15 nm) *via* intra-*cisterna magna* administration, with tracking by SPECT imaging. To accelerate CSF brain influx, we administered AuNPs intracisternally in conjunction with systemic hypertonic saline, which dramatically increased the parenchymal AuNP uptake, especially in deep brain regions. AuNPs entered the CNS along periarterial spaces as **visualized** by MRI of gadolinium-labelled AuNPs and were cleared from brain within 24 **h** and excreted through the kidneys. Thus, the glymphatic-assisted perivascular network augment by systemic hypertonic saline is a pathway for highly efficient brain-wide distribution of small AuNPs.

1. Introduction

The human and societal costs of disorders affecting the central nervous system (CNS) are steeply rising and novel treatments are urgently needed [1]. While many potential medications have hindered CNS access due to the blood-brain barrier (BBB), nanoparticles are a promising solution to improve the efficacy and safety of drugs targeting the CNS [2]. Nanoparticles typically range in size from 1 to 100 nm, thus one hundredth the diameter of a typical neuron and quite invisible to light microscopy. Their structure and composition can be modified to influence their pharmacokinetics, and ultimately that of their drug cargo. Integration in nanoparticles can improve drug stability, target accumulation and exposure duration, thus potentiating the therapeutic effect. Indeed, nanoparticles can be tailored to deliver a variety of drugs, including biological macromolecules, as well as hydrophobic and hydrophilic drugs of relatively low molecular weight [3].

While nanoparticles possess many intriguing features, their size and surface properties tend to hinder their transit across the BBB, which limits their effectiveness by intravenous administration [4,5]. Even the smallest nanoparticles, specifically designed to cross the BBB, have had

limited brain uptake, generally in the range of 0.1% of injected dose per gram (%ID/g) [5]. Administering drugs directly to the cerebrospinal fluid (CSF) by intrathecal injection circumvents the BBB endothelium, and this approach may be particularly useful for nanoparticles, which are better retained in the CNS compared with small-molecular weight drugs [2]. However, the large size of nanoparticles, as with antibodies, tend to hinder their flux from the subarachnoid space to deep CNS structures [6].

Recent findings on the glymphatic system bring exciting new prospects [7] for improving the CNS delivery of intrathecally administered nanoparticles. The glymphatic pathway is a physiologically modulated CNS-wide fluid transport system, which facilitates the flow of CSF from periarterial spaces of penetrating arteries into the deep brain regions and through the brain parenchyma to clear the brain interstitium of metabolic waste [8,9]. Compared with the awake state, glymphatic CSF transport increases during natural slow-wave sleep [10] and under certain anesthetic regimens [11–13]. In addition, an increase in plasma osmolarity following systemic administration of mannitol or hypertonic saline transiently boosts periarterial CSF influx [14,15]. Hypertonic treatment enhanced binding of an intracisternally administered antibody against amyloid-β in mice [14] and the delivery of lumbar intrathecal morphine to the spinal cord [16], suggesting that hypertonic treatment could generally serve as an adjuvant to improve CNS distribution of various intrathecally delivered drugs.

Here, we administered small gold nanoparticles (AuNPs) labelled with the low energy gamma-emitter indium-111 (^{111}In) or the magnetic resonance imaging (MRI) contrast agent gadolinium (Gd) to the intrathecal space of rats; the dynamic distributions were then imaged using single-photon emission tomography (SPECT) or MRI, respectively. We tested the hypothesis that hypertonic saline would enhance the global CNS delivery of intrathecal AuNPs within periarterial spaces of penetrating arteries, leading to increased intracranial exposure and marked increase in the distribution of AuNPs to deep brain structures. We also followed the delayed elimination of the small AuNPs from the brain *via* lymphatic structures and their ultimate excretion through the kidneys, without significant accumulation in non-target body organs, which rendered insignificant their accumulation in the liver and other organs. Thus, we undertook preclinical imagines studies to test the fitness of glymphatic-assisted intrathecal delivery as a novel strategy for the widescale delivery of AuNPs to the brain and the spinal cord.

2. Methods

2.1. Animals

All procedures were approved by the local authorities (Animal Experiments Council under the Danish Ministry of Environment and Food, 2015-15-0201-00535). Experiments complied with the ARRIVE guidelines [17] and the EU Directive 2010/63/EU on the protection of animals used for scientific purposes. Fifty-one male Sprague-Dawley rats (200–300 g, Charles River, Salzburg, Germany) were used. They were housed in groups of four in individually ventilated plastic cages in light- and temperature-controlled rooms. Water and standard laboratory pellets were available *ad libitum*.

2.2. Materials

All chemicals were used without further purification. All chemicals were purchased from Sigma-Aldrich, except LA-DOTA (2,2′,2″-(10-(2-((2-(5-(1,2-dithiolan-3-yl)pentanamido)ethyl)amino)-2-oxoethyl)-1,4,7,10-tetraazacyclododecane-1,4,7-triyl)triacetic acid) which was purchased from CheMatech (F), and [^{111}In]InCl₃ which was bought from Curium Netherlands B.V. (NL). For the synthesis of the ^{111}In-LA-DOTA complex, ultratrace water (Sigma-Aldrich) was used as a solvent, but Milli-Q water (Millipore, USA) was used in all other chemical procedures. Ultraviolet-visible spectroscopy (UV-VIS) data were collected on a

Shimadzu UV-1800 UV/VIS Scanning Spectrophotometer. AuNPs were characterized by dynamic light scattering (DLS), providing hydrodynamic diameters. The size was measured five times in each sample and reported as mean square displacement (MSD) calculated number-weighted averages. DLS measurements were carried out in the reaction mixture medium without dilution (sodium citrate and Milli-Q water) at 25 °C. DLS and Zeta potential measurements were done using a Brookhaven Instruments ZetaPALS apparatus. Inductively coupled plasma optical emission spectroscopy (ICP-OES) measurements were performed with a Thermo Scientific iCAP 7000 Plus Series ICP-OES apparatus.

The size distribution of the AuNPs was also estimated by analyzing a collection of TEM images acquired with an FEI S/TEM 80–300 kV Analytical Titan microscope operating at 300 kV. The nanoparticles suspended in citrate solution (6.5 mM) were drop casted onto a regular copper grid with a Holey carbon membrane by using a microliter pipette. Radio-TLC plates (normal phase, eluent = methanol:water 50:50 with 4% ammonium acetate) were analyzed using a Ray test MiniGita apparatus equipped with a beta detector Geiger-Muller Counter, or a Perkin Elmer Cyclone® Plus Storage Phosphor System. Radioactivity was quantified with either a CRC®-55tR dose calibrator (activities higher than about 1 MBq) or Hidex 300 SL Automatic TDCR Liquid Scintillation Counter (for activities below about 1 MBq). For the liquid scintillation counting (LSC) measurements, we prepared a standard curve based on ^{111}In, for which all samples fell within the linear range (see Supplementary Information S1).

2.3. Synthesis of AuNPs

All glassware was thoroughly rinsed with aqua regia (1:3, 65% HNO₃: 32% HCl) and dried before use. Small AuNPs were prepared according to a modified literature procedure [18]. Freshly prepared aq. trisodium citrate (7.5 mL, 33 mM, 0.25 mmol) was mixed with water (30 mL), aq. K₂CO₃ (250 μL, 150 mM, 38 μmol) and aq. tannic acid (30 μL, 2.5 mM, 75 nmol). The resulting solution was stirred while heated to 70 °C. Aq. HAuCl₄ (250 μL, 25 mM, 6.25 μmol) was added, leading to the mixture assuming a grey colour, followed by a gradual change to orange–red. The mixture was stirred at 70 °C for 15 min and then allowed to cool to room temperature, furnishing small, citrate-stabilized AuNPs (Au concentration = 0.032 mg/mL). The size of the AuNPs was assessed by UV–Vis, showing a maximum absorption at 507 nm, corresponding to a diameter of 4 nm [18] and DLS, giving a number-weighted mean diameter of 4.3 ± 0.4 nm (polydispersity index, PDI 0.40 ± 0.11).

For conducting further analyses as well as for further use in stability studies, a part of the citrate-stabilized AuNPs (14 mL) was mixed with a freshly prepared aq. solution of methoxy PEG₂₀₀₀ thiol (mPEG₂₀₀₀-SH, 4.0 mg/mL, 200 μL, 800 μg) and stirred at room temperature for 15 min. DLS analysis showed an increase in size to 10.6 ± 2.5 nm (PDI 0.34 ± 0.08) indicating successful coating. The PEG₂₀₀₀ coated AuNPs were also analyzed by TEM, giving an average size of 3.6 ± 0.5 nm. For stability studies, 7.0 mL of PEG₂₀₀₀ coated AuNPs were filtered on a 30 kDa cutoff Amicon centrifugation cartridge and resuspended in isotonic HEPES buffer (1000 μL, Au concentration = 0.224 mg/mL).

2.4. Synthesis of ^{111}In-LA-DOTA

Aqueous (aq.) LA-DOTA (20 μL, 0.5 mM, 10 nmol) was mixed with [^{111}In]InCl₃ (in 20 mM aq. HCl, 280 μL, 250 MBq) and aq. sodium acetate (500 μL, 30 mM). The pH of the resulting solution was 6.0. The solution was heated to 90 °C for 20 min to produce the ^{111}In-LA-DOTA stock solution. After cooling, 250 μL of the ^{111}In-LA-DOTA stock solution was removed and mixed with aq. NaCl (50 μL, 0.53 mM) and an isotonic HEPES buffer (300 μL, 10 mM HEPES, 150 mM NaCl, pH 7.5) to provide the ^{111}In-LA-DOTA free complex solution. The activity of this solution was 0.122 MBq/μL. For the synthesis scheme, see Supplementary Information S2.

2.5. ^{111}In-radiolabeling of AuNPs

^{111}In-LA-DOTA stock solution (550 μL) was mixed with a dispersion of citrate-stabilized AuNPs (7.0 mL, Au concentration = 0.032 mg/mL). The mixture was stirred for 20 min at room temperature, while the attachment to the AuNPs was monitored by radio-TLC. A freshly prepared aq. solution of methoxy PEG$_{2000}$ thiol (mPEG$_{2000}$-SH, 4.0 mg/mL, 100 μL, 400 μg) was then added, followed by stirring at room temperature for 15 min. Analysis by UV-VIS spectrophotometry showed a red shift of the maximum absorption to 516 nm, corresponding to a particle diameter of 9 nm, while DLS analysis gave a mean, number-weighted diameter of 12.26 ± 2.30 nm (PDI 0.50 ± 0.07), both indicating successful coating. The Zeta potential of the ^{111}In-labelled AuNPs was −1.79 ± 0.92 mV. Analysis by radio-TLC showed that 80% of the radioactivity was associated with the AuNPs. The ^{111}In-AuNPs were purified on a 30 kDa cutoff Amicon centrifugation cartridge. The resulting activity associated with the ^{111}In-AuNPs was 132 MBq while 48 MBq were found in the filtrate, corresponding to a radiochemical yield of 73%. Isotonic HEPES buffer (7.0 mL) was added to wash the ^{111}In-AuNP-containing filtrand, followed by centrifugation. After this washing step, 128 MBq remained associated with the ^{111}In-AuNPs. The ^{111}In-AuNPs were resuspended in isotonic HEPES buffer (600 μL) yielding a radioactivity concentration of 0.213 MBq/μL and an Au concentration of 0.373 mg/mL.

2.6. Synthesis of Gd-LA-DOTA

LA-DOTA (100 μL, solution 4.0 mM, 400 nmol) was added to an acid-washed HPLC vial. GdCl$_3$ (40 μL, solution 10 mM, 400 nmol) was added, followed by ammonium acetate (100 μL, solution 100 mM) and water (760 μL). The pH of the solution was 6.5. The solution was heated to 85 °C for 45 min and left to cool down to room temperature, giving the Gd-LA-DOTA complex solution. For the synthesis scheme, see Supplementary Information S2.

2.7. Gd-labelling of AuNPs

A dispersion of citrate-stabilized AuNPs (380 mL) with composition and concentration similar to the batch used in the synthesis of the ^{111}In-AuNPs (gold concentration = 0.032 mg/mL) was prepared. (DLS analysis showed a number weighted nanoparticle diameter of 2.7 ± 1.4 nm and UV–visible spectrum gave a maximum of the absorption band at 506 nm, corresponding to a size of 3.5 nm). The Gd-LA-DOTA complex solution (whole batch, 1000 μL) was added to the citrate coated AuNPs dispersion. The mixture was stirred at room temperature for 30 min. A freshly prepared aq. solution of methoxy PEG$_{2000}$ thiol (mPEG$_{2000}$-SH, 4.0 mg/mL, 6.0 mL, 24.0 mg) was then added, followed by stirring at room temperature for 20 min (DLS analysis showed a number weighted mean diameter of 10.5 ± 2.0 nm (PDI 0.41 ± 0.10). The Zeta potential of the Gd-labelled AuNPs was −0.12 ± 0.34 mV). The Gd-labelled AuNPs were then filtered on a 30 kDa cutoff Amicon centrifugation cartridge, washed with 10 mL of isotonic HEPES buffer, and resuspended in a final total volume of 500 μL (volume adjustment done with addition of isotonic HEPES buffer). The Au and Gd concentrations in the final sample were measured by ICP-OES: Au, 24.65 mg/mL; Gd, 0.058 mg/mL. This corresponds to a Gd-labelling yield of 47%.

2.8. Stability of labelled AuNPs in brain homogenate and CSF

To obtain CSF and brain homogenate (BH) for assessing AuNP stability *in vitro*, rats were anesthetized with subcutaneous ketamine (100 mg/kg) and dexmedetomidine (0.5 mg/kg) and fixed to a stereotaxic frame after verification of loss of response to painful stimuli. The cisterna magna was exposed, and CSF was carefully drawn using a syringe and a 30G needle. The rats were then euthanized, and the brains were quickly removed and cut in four quarters. Each quarter portion was mixed in 5 mL phosphate-buffered saline (PBS) using a homogenizer. The CSF and BH samples were stored at −80 °C. To allow UV-VIS characterization at low radioactivity levels, ^{111}In-AuNPs were mixed with non-radiolabelled, PEG$_{2000}$-coated AuNPs from the same batch. The gold concentration was the same in both AuNPs samples (0.373 mg/mL). Plastic size exclusion chromatography (SEC) cartridges (4 cm) were packed with Sephacryl® S300HR, as has been previously used for tissue stability studies on nanoparticles [19,20]. PBS was used as eluent. First, samples of pure ^{111}In-AuNPs or ^{111}In-LA-DOTA free complex (both: 100 μL) were applied to these cartridges and separated into 1 mL fractions to give the $t = 0$ samples. Radioactivity levels in the eluted fractions were monitored, and UV-VIS spectra (200–800 nm) were recorded. Samples were also analyzed by radio-TLC. The same procedure was then applied to mixtures of ^{111}In-AuNPs or free ^{111}In-LA-DOTA mixed with CSF or BH.

2.8.1. ^{111}In-AuNPs

The following mixtures were prepared and analyzed: 1) Cerebrospinal fluid (175 μL) + AuNP dispersion (175 μL) and 2) BH (87 μL) + PBS (88 μL) + AuNP dispersion (175 μL). 1% antibiotic was added to each vial. The mixtures were incubated at 37 °C and samples were analyzed by SEC at 4, 24, and 48 h (Supplementary Information S3). The experiment was performed in triplicate.

2.8.2. Free ^{111}In-LA-DOTA

The following mixtures were prepared and analyzed: 1) CSF (30 μL) + ^{111}In-LA-DOTA complex solution (30 μL), 2) BH (15 μL) + PBS (15 μL) + ^{111}In-LA-DOTA complex solution (30 μL). 1% antibiotic (antibiotic antimycotic solution (100×), stabilized with 10,000 units penicillin, 10 mg streptomycin and 25 μg amphotericin B per mL) was added to each vial. The mixtures were incubated at 37 °C and samples were analyzed by radio-TLC at 0, 4, 24, and 48 h. The experiment was performed in triplicate.

2.8.3. Biological controls

Neat CSF (50 μL) and BH (25 μL + 25 μL PBS) were analyzed and the UV-VIS spectrum recorded for each fraction, as above.

2.8.4. ^{111}In-LA-DOTA tissue association control

The following mixtures were prepared: 1) free ^{111}In-LA-DOTA complex solution (75 μL) + cerebrospinal fluid (75 μL) and 2) free ^{111}In-LA-DOTA complex solution (75 μL) + BH (37 μL) + PBS (38 μL). After 1.5 h, 100 μL of each mixture was withdrawn and analyzed by SEC as above. For each fraction collected, the radioactivity as well as the UV–visible spectrum between 200 and 800 nm was measured. For raw data, see Supplementary Information S4.

2.9. Intracisternal cannulations and AuNP infusions

Cisterna magna cannulation was performed as previously described with minor modifications [21]. Rats were anesthetized with a mixture of ketamine (100 mg/kg) and dexmedetomidine (0.5 mg/kg), administered subcutaneously in a volume of 2 mL/kg. After verification of loss of response to toe pinch, animals were placed in a stereotaxic frame with the neck flexed (30°). The atlanto-occipital membrane overlying the cisterna magna was surgically exposed and a 30G short-beveled dental needle connected to PE10 tubing was carefully inserted into the intrathecal space. The catheter was fixed to the dura with cyanoacrylate glue and dental cement.

For post-operative analgesia, rats that were imaged for 24 h received 5 mg/kg carprofen (Rimadyl® vet, 50 mg/mL, Orion Pharma, Espoo, Finland) s.c. at the beginning of surgery. Temperature was monitored and normothermia was maintained with a heating pad. Nanoparticles or the ^{111}In-LA-DOTA conjugate were infused into the cisterna magna at a rate of 1.6 μL/min using a KD Scientific Legato® 130 pump (Holliston, MA, USA) attached to a Hamilton Gastight 1700 microsyringe (Bonaduz,

Switzerland). The total volume of 32 μL was infused over 20 min. Five minutes before the AuNP infusion started, rats received either HTS (1 M, 20 mL/kg i.p.) or isotonic saline (0.154 M, 20 mL/kg i.p.). In the MRI experiments, all rats received a HTS, and the infusion rate of Gd-labelled nanoparticles was the same as above, but with a greater total infusion volume of 80 μL.

2.10. Single-photon emission tomography (SPECT) and computerised tomography (CT)

Radioactivity of the infused dose was measured with VIK-202 dose calibrator (Comecer, Joure, The Netherlands). The VECTor4CT (MILabs, Utrecht, Netherlands) system was used for SPECT/CT imaging. SPECT images were acquired with a high energy ultra-high resolution rat clustered multi-pinhole collimator (HE-UHR-RM, pinhole diameter 1.8 mm). Acquired images were reconstructed using Similarity-Regulated Ordered Subsets Estimation Maximization (SROSEM) with a voxel size of 0.6 mm and 5 iterations. Both decays at the ^{111}In photopeaks ($\pm$20%) and background at 20% outside each photopeak window) were individually used for the reconstruction. Two highly accurate energy dependent system matrices for iterative image reconstruction (SROSEM [22]) were used to minimize anisotropic blurring artifacts in ^{111}In imaging with high local uptake and no background activity in surrounding structures. In each matrix the effects of energy dependent pinhole penetration (calculated using ray tracing [23]) and intrinsic detector resolution with depth-of-interaction (DOI) effects in the crystal were modelled. The DOI effect was calculated using GATE Monte Carlo simulations [24], which were stored in tables and used in the raytracer. Matrices were generated for 171 keV and 245 keV photons and were used during the reconstruction from projections of the corresponding energy peaks. The resulting SPECT images were then added and averaged to obtain the final ^{111}In image. Head and full-body CT images were acquired directly after the SPECT scans in the same imaging session. SPECT data were attenuation corrected, decay corrected to the half-life of ^{111}In, and corrected for injected activity, with each voxel representing the percentage of the injected dose per cm^3 (%ID/cm^3).

2.11. SPECT analysis

Head and full-body CT images from each imaging session were nonlinearly registered using Advanced Normalization Tools (ANTs) to the appropriate population-based CT template (described below). Regions of interest (ROIs) were then either drawn manually on individual CT images, manually in the template space, or were computed automatically in the case of the delineation between CSF and brain described below. Manual ROIs were drawn using ITK-SNAP software. Spherical ROIs (diameter 1.4 mm) for striatum and thalamus were placed using an MRI-based in-house brain template as reference (described below). Spherical ROIs for nasal turbinates, pharyngeal lymph vessels, and deep cervical lymph nodes were drawn using head CT template as reference and the gross average of all head SPECT images as reference for the deep cervical lymph nodes (Fig. 5a shows an illustration of the placement). Full-body CTs were segmented into the intracranial compartment, spine, kidneys, bladder and lungs, and a spherical ROI (Ø12 mm) was placed in the liver. Time-activity-curves and descriptive statistics were calculated for each ROI using MATLAB 2019B. Soft tissue regions that could not be delineated using CT images (spherical ROIs) were quantified as percentage of the injected dose per cm^3 (%ID/cm^3), and other regions were quantified as %ID. Group-wise SPECT image time-series were averaged from the SPECT images after registration to template spaces to allow visualization of mean tracer distribution.

2.12. Magnetic resonance imaging (MRI)

MRI was carried out on a Bruker BioSpec 94/30 USR magnet interfaced with a Bruker Advance III console controlled by Bruker ParaVision

v. 6.0.1 (Bruker BioSpin, Germany). A volume RF-coil (86 mm) was used for transmission along with a 4-channel phased array surface RF receiver coil (Bruker BioSpin, Germany). Dynamic contrast-enhanced MRI (DCE-MRI) consisted of sequential frames of a 3D spoiled gradient echo sequence (FLASH3D, TE: 3.13 ms, TR: 15.8 ms, matrix: 280 × 173 × 380, voxel size: 0.1 × 0.15 × 0.1 mm, FA: 20). Two frames were acquired prior to contrast agent infusion (20 min), and 18 frames post-infusion (180 min). Rectal temperature and respiratory rate were monitored continuously for the duration of experiment using an MRI-safe monitoring system (SA Instruments, New York, USA).

2.13. MRI analysis

DCE-MRI sequences were rigidly motion-corrected using ANTs, and the brain was extracted by registration to the MRI brain template. ROIs were manually drawn in the perivascular spaces around the middle cerebral artery, and the contrast-enhancement signal was calculated as the percentage change from the pre-contrast baseline ($\Delta S/S_0$).

2.14. Population-based MRI and CT templates

To aid and standardize analysis and visualization of SPECT data, we used population-based average templates of full-body and head-focused CT as well as of T2-weighted brain MRI. CT templates were created from CT data acquired for this study, while the MRI template was created from the MRI from a group of separate rats (12 Sprague-Dawley rats, 7 males, 225–400 g, ketamine/dexmedetomidine anesthesia (100/0.5 mg/kg)) that had served as control subjects in other studies. Population-based average head CT, body CT and brain MRI templates were created separately using a modified version of the pipeline described by Avants et al. [25] using ANTs. A representative scan from each included animal was used (full-body CT: $n = 42$, head CT: $n = 21$, brain MRI: $n = 12$). First, a voxel-wise average was calculated of all scans, resulting in the initial template; then, all scans were registered to the initial template and a new voxel-wise average was calculated to produce the next iteration of the template. This process was repeated with increasingly complex registration steps (rigid, affine, and nonlinear), repeating each step until there was little change from between iterations. Full body CT images were thresholded at 500 Hounsfield units (HU) before the template building process. T2-weighted MRI was acquired using the same setup as the dynamic contrast-enhanced MRI; imaging consisted of T2-weighted TurboRARE (TE: 24.1 ms, TR: 16 s, Echo spacing: 8.033, RARE factor: 8, matrix: 375 × 250, FOV 30 × 20 mm, in-plane resolution: 0.08 × 0.08 mm, 128 slices, 220 μm slice thickness, 110 μm overlap, 8 repetitions). Eight serial images from each animal were rigidly motion corrected, averaged, and bias-field corrected using the N4 software [26]. Affine registrations between the three templates were calculated semi-automatically using ITK-SNAP software v. 3.8.0. The intracranial space was manually segmented using ITK-SNAP and tissue segmentation of the intracranial space into brain tissue and CSF was computed from the MRI template using Advanced Normalization Tools (ANTs) Atropos [27] based on an initial manual threshold.

2.15. Statistics and software

Image preprocessing was carried out using Python 3.8.5 and image registration, bias field-correction, and automated image segmentation were performed with ANTs. Extraction of time-activity-curves and derived statistics was carried out using MATLAB 2019B. Unless otherwise noted, measurements were reported as mean ± standard deviation, and statistical comparison consisted of unpaired *t*-test in the case of two groups and ordinary one-way ANOVA with Dunnett's multiple comparisons test in the case of several groups. Statistical tests were carried out using GraphPad Prism 9.2.0.

3. Results

3.1. Synthesis and characterization of small gold nanoparticles

We prepared small AuNPs coated with polyethylene glycol (PEG$_{2000}$) and labelled with either ^{111}In for imaging by SPECT or Gd for MRI, respectively (Fig. 1a). Citrate-stabilized, uncoated AuNPs were first formed by reduction of HAuCl$_3$ solutions. To demonstrate complete conversion of the added gold to AuNPs, aliquots were filtered on a 3000 Da filter cartridge and the clear, non-AuNP containing filtrate was analyzed by ICP-OES. No remaining dissolved gold could be detected in these mixtures, meaning that the concentration was lower than the detection limit (<5 µg/L) and that the AuNP formation was quantitative. In addition, the gold content of Gd labelled AuNPs was measured by digestion in aqua regia followed by gold determination by ICP-OES, which confirmed that the originally added HAuCl$_3$ had been converted quantitatively to AuNPs. The prepared AuNPs were then labelled and coated with polyethylene glycol (PEG$_{2000}$, Fig. 1a, top). Labelling was achieved *via* complexation of ^{111}In^{3+} or Gd^{3+} with a conjugate of lipoic acid (LA) and the macrocyclic chelator 1,4,7,10-tetraazacyclododecane-1,4,7,10-tetraacetic acid (DOTA). The functional group DOTA is a well-established chelator used in medical imaging, which provides stable complexes for both In^{3+} [28] and Gd^{3+} [29]. The chelates were synthesized first (Supplementary Information S2), whereupon they were attached to the AuNPs *via* interaction of the disulphide moiety with the gold particle surface (Fig. 1a, bottom). This procedure was followed by

saturation of the AuNP surface with methoxy-PEG$_{2000}$ thiol, to provide the final ^{111}In-AuNPs or Gd-AuNPs for use *in vivo*.

The prepared AuNPs were characterized by dynamic light scattering (DLS), showing hydrodynamic diameters of 4.3 ± 0.9 nm for the citrate-stabilized, uncoated AuNPs before PEG$_{2000}$ coating and 12.3 ± 2.3 nm (^{111}In) or 10.5 ± 2.0 nm (Gd) after labelling and PEG$_{2000}$ coating. Transmission electron microscopy (TEM) showed gold core diameters of 3.6 ± 0.5 nm (mean ± SD, $n = 264$) (Fig. 1b, Supplementary Information S5). As a further measure of size, both uncoated and PEG$_{2000}$-coated AuNPs were analyzed by UV-VIS spectroscopy, with a maximal absorption at 507 nm for uncoated AuNPs and 516 nm for PEG$_{2000}$-coated AuNPs, which indicated diameters of 4 nm and 9 nm, respectively [18] (Fig. 1c).

We first studied the stability of the labelled AuNPs by incubation *in vitro* in CSF and BH, both media being highly relevant for the investigated delivery route. To enable facile quantification by radioactivity measurements, we used ^{111}In-AuNPs for these experiments. The incubated mixtures were monitored for detachment of the label from the AuNP surface for 48 h, *via* separation of AuNPs and the detached small-molecular weight chelate by size exclusion chromatography (SEC) on a Sephacryl S300HR resin.

For each Sephacryl eluted fraction, we measured radioactivity concentration in Bq and optical absorption at 515 nm (AuNP local maximum) (Fig. 1d, Supplementary Information S3). At the start, approximately 95% of the ^{111}In-LA-DOTA radioactivity was associated with the AuNPs at $t = 0$. At four hours, 13% (CSF) and 11% (BH) of ^{111}In-
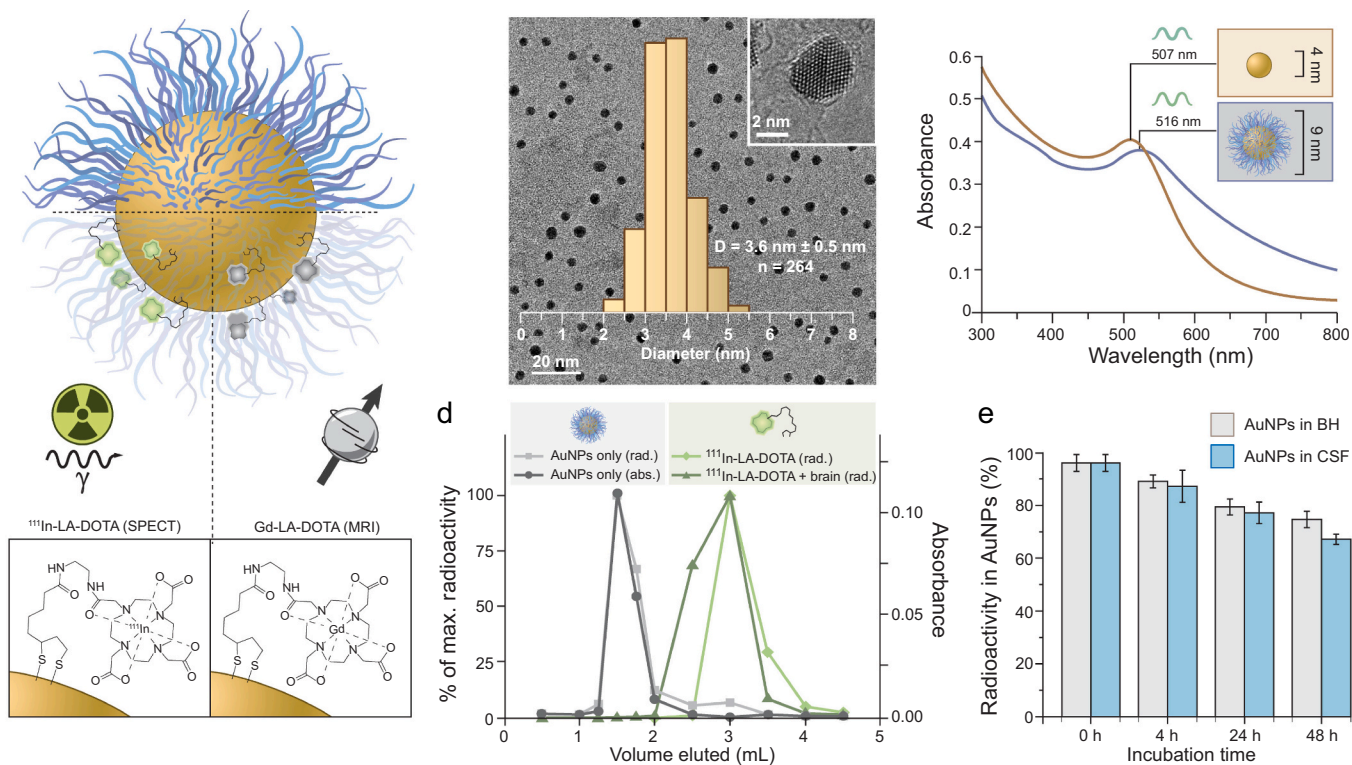

Fig. 1. Preparation of small gold nanoparticles to be visualized with either single-photon emission tomography (SPECT) or magnetic resonance imaging (MRI). a, Schematic illustration of a PEG$_{2000}$ coated AuNP, labelled with ^{111}In-LA-DOTA (bottom left) or Gd-LA-DOTA (bottom right). b, Background: Transmission electron microscopy (TEM) image of PEG$_{2000}$ coated AuNPs. Insert: High resolution image of a single AuNP. Front: Size distribution of PEG$_{2000}$ coated AuNPs measured by TEM. c, Representative UV-VIS spectra of citrate-stabilized (brown) and PEG$_{2000}$ coated (blue) AuNPs. d, SEC separation of selected sample mixtures. ^{111}In-AuNPs: Absorption at 515 nm (dark grey, right axis) and gamma radioactivity (light grey, left axis). Free ^{111}In-LA-DOTA complex: Gamma radioactivity (light green, left axis). ^{111}In-LA-DOTA was mixed with brain homogenate for 1.5 h: Radioactivity (dark green, left axis). e, Stability of ^{111}In-LA-DOTA labelled AuNPs in rat brain homogenate (BH, grey) or rat CSF (blue) at 37 °C, depicted as percentage of the maximal radioactivity associated with the AuNP fraction after SEC separation. The $t = 0$ data was obtained immediately before mixing with the tissue extracts or CSF. Errors are shown as standard deviation ($n = 3$). abs., absorption; AuNP(s), gold nanoparticle(s); CSF, cerebrospinal fluid; ^{111}In-AuNPs, ^{111}Indium-labelled gold nanoparticles; ^{111}In-LA-DOTA, ^{111}Indium-labelled conjugate (lipoic acid–1,4,7,10-tetraazacyclododecane-1,4,7,10-tetraacetic acid); PEG, polyethylene glycol; rad., radioactivity; SEC, size exclusion chromatography. (For interpretation of the references to colour in this figure legend, the reader is referred to the web version of this article.)

LA-DOTA had been detached from the AuNPs, which increased slightly to 23% (CSF) and 20% (BH) at 24 h, and 33% (CSF) and 25% (BH) at 48 h (Fig. 1e, Supplementary Information S3). As control samples, we incubated free ^{111}In-LA-DOTA in both CSF and BH samples at 37 °C and monitored its decomposition by Sephacryl chromatography and by radio thin layer chromatography (radio-TLC, Supplementary Information S4 and S6). The results demonstrated that free ^{111}In-LA-DOTA did not bind to any large molecular weight components of the CSF and BH samples, which might otherwise could have provided false positive results in the tests of AuNP stability (Fig. 1d). There was no sign of release of ^{111}In from the chelator during 48 h, consistent with earlier reports of the high stability of the ^{111}In-LA-DOTA complex in biological media [28,30,31]. This further supported our interpretation that the observed release of radioactivity stemmed from detachment of the ^{111}In-LA-DOTA complex from the AuNP surface, which should generalize to the Gd-labelled variant for MRI tracking.

3.2. Systemic hypertonic saline enhances brain-wide distribution of small gold nanoparticles

We used SPECT imaging to follow dynamically the distribution and elimination of ^{111}In-LA-DOTA labelled AuNPs (^{111}In-AuNPs) infused to the CSF-filled cisterna magna (Fig. 2a). Five minutes prior to AuNP infusion (32 µl, 2.2 ± 0.7 MBq, 1.6 µl/min), anesthetized Sprague-Dawley rats received a slow intraperitoneal injection of either hypertonic saline (HTS, 1 M, 20 ml/kg, 40 mOsm kg^{-1}) or isotonic saline (vehicle; VEH, 0.154 M, 20 ml/kg) (Fig. 2b). To enable visualization and quantification at the group level, head-focused SPECT and computed tomography (CT) images obtained on the same scanner were registered to a common coordinate system for rat brain using an MRI-derived template as reference.

In both treatment groups, the ^{111}In-AuNP dispersion flowed from the cisterna magna through the subarachnoid space along surface arteries to the circle of Willis and further along the posterior, middle, and anterior cerebral arteries, much as previously reported for other CSF tracers [32] (Fig. 2c). While ^{111}In-AuNP availability as a percentage of injected dose (%ID) in brain peaked at comparable amounts, the residual ^{111}In-AuNP mass at 180 min after the start of the infusion was doubled with HTS treatment, which significantly increased the overall intracranial ^{111}In-AuNP exposure during the first three hours (AUC$_{0-3h}$) of the SPECT recording by 40% (Fig. 2d–e).

Using an MRI-derived template derived from a separate group of rats of the same strain and age, we roughly divided the intracranial compartments into brain parenchyma and CSF, to give an approximate depiction of which compartment was responsible for the increase in intracranial ^{111}In-AuNP exposure. Due to the small size of the rat subarachnoid and perivascular spaces, compounded by the relatively low spatial imaging resolution of the SPECT technique, there was significant signal spill-over between the brain parenchyma and CSF in the intracranial compartment. From the time-activity-curves measured for brain and CSF (Fig. 2f–g), the increased ^{111}In-AuNP exposure appeared to arise largely in the brain parenchyma. To confirm this, we compared the ratios of brain exposure to the intracranial exposure (AUC$_{0-3h\ brain}$: AUC$_{0-3h\ intracranial}$) between groups, which revealed higher ratio in the HTS compared with the isotonic vehicle group (VEH: 0.565 ± 0.018, HTS: 0.624 ± 0.021, $p = 0.0001$, t-test), which further implied that HTS treatment enhanced the delivery of ^{111}In-AuNPs to the brain.

In addition to validating the radiolabel stability of the ^{111}In-AuNPs *in vitro* (Fig. 1e), we compared the *in vivo* distribution of the free ^{111}In-LA-DOTA low-molecular weight linker with that of ^{111}In-AuNPs in rats that had received intraperitoneal isotonic saline (VEH). While the overall intracranial AUC$_{0-3h}$ of the ^{111}In-AuNPs and the low-molecular weight conjugate did not differ (Fig. 2e), the conjugate showed higher penetration to the brain (Fig. 2f), suggesting size-dependent brain penetration of these tracers from the cisterna magna, as has been previously demonstrated [8].

To further examine the penetration of ^{111}In-AuNPs to the brain parenchyma, we measured radioactivity in deep brain regions, relatively unaffected by spill-over signal from the CSF. Using the MRI template as an anatomical guide, we placed small spherical regions of interest (ROIs) (diameter 1.4 mm) centrally in the bilateral caudate putamen (Fig. 3a–b) and thalamus (Fig. 3c–d) to measure dynamically the ^{111}In-AuNP concentrations. HTS increased the exposure (AUC$_{0-3h}$) to ^{111}In-AuNPs by 3.7-fold in the striatum (Fig. 3b) and 12-fold in the thalamus (Fig. 3d), respectively, demonstrating a dramatically enhanced deep brain penetration with HTS pretreatment.

3.3. Brain-wide periarterial distribution of small gold nanoparticles imaged with dynamic contrast-enhanced magnetic resonance imaging

Since SPECT imaging has limited spatial resolution to visualize the exact delivery routes of tracer, we next performed dynamic contrast-enhanced MRI (DCE-MRI) using gadolinium-labelled AuNPs (Gd-AuNPs) as a contrast agent (Fig. 4a). To compensate for the lesser target sensitivity of MRI as compared with SPECT, we increased the infused volume of Gd-AuNPs to 80 µL [32] while maintaining the same infusion rate, which has been shown to not influence intracranial pressure even during prolonged intracisternal infusion episodes [33]. As usual, the infusion was initiated five minutes after the administration of systemic HTS (Fig. 4b). Dynamic MRI imaging affirmed the brain-wide distribution of Gd-AuNPs in the perivascular spaces of arteries in pial arteries (Fig. 4c–d). Periarterial Gd-AuNP concentration measured in the perivascular space of the left middle cerebral artery showed a marked peak at 78 ± 32 min, followed by a gradual decrease to $39 \pm 17\%$ of the peak at 180 min (Fig. 4e). Importantly, Gd-AuNPs were clearly detected in the periarterial spaces of penetrating arteries (Fig. 4f). We noticed a decrease in the MR-signal of brain tissue following the HTS injection, which we ascribed to a general decrease in the parenchymal water content under hypertonic conditions [14]. As a result, we were not able to quantify the MRI signal increase in the brain parenchyma caused by the presence of Gd-AuNPs.

3.4. Hypertonic saline decreases the egress of intrathecally administered small gold nanoparticles to lymphatic structures

Next, we measured ^{111}In-AuNP transport along CSF egress routes (Fig. 5a–b). HTS treatment did not significantly change peak concentrations or exposure in the cervical spine (Fig. 5c). In line with the enhanced deep brain uptake, the egress of ^{111}In-AuNPs through the nasal turbinates [34] (Fig. 5d), the pharyngeal lymphatic pathway [35,36] (Fig. 5e), and deep cervical lymph nodes (Fig. 5f) was significantly reduced by HTS. These findings suggest that HTS mainly reduces shunting of ^{111}In-AuNPs from the CSF to lymphatic structures, without significant effects on their caudal-directed flow in the spinal canal.

The ^{111}In-AuNP concentration both in the VEH and HTS group peaked approximately simultaneously in the nasal turbinates and cervical lymph nodes. While the nasal route is an important route of CSF egress [34], our observation that ^{111}In-AuNP signals arrived simultaneously at the nasal turbinates and cervical lymph nodes may suggest that egress routes from the intracranial compartment to the cervical lymph nodes may be faster or more direct than through nasal turbinates. Potential direct routes to deep cervical lymph nodes could include egress through the meningeal lymphatic vessels on the ventral side of the brain [37] or *via* cranial nerve sheaths, as visualized *in vivo* in mice by Stanton et al. [35].

We also used SPECT to assess the kinetics of the free ^{111}In-LA-DOTA conjugate in the efflux pathways. Although the intracranial AUC$_{0-3h}$ did not differ between the conjugate and ^{111}In-AuNPs (Fig. 2e), exposure to ^{111}In-AuNPs in the nasal turbinates was significantly higher than with free ^{111}In-LA-DOTA (Fig. 5d), possibly suggesting a more important role of the nasal outflow routes for large molecules or particles. Importantly, the ^{111}In-LA-DOTA conjugate was virtually undetectable in the deep lymph nodes (Fig. 5f), suggesting that exposure of the lymphatic

structures of the head and neck after intrathecal administration of low-molecular weight agents is minor, and that pharmacologic targeting of these lymphatic structures could perhaps be facilitated using nanoparticles as drug carriers. The dramatically different kinetics of ^{111}In-LA-DOTA-AuNPs and free ^{111}In-LA-DOTA conjugate in the efflux pathways furthermore indicate tracer stability *in vivo*, in accord with our findings above that the ^{111}In-LA-DOTA-AuNP radiolabel is stable *in vitro*.

3.5. Small gold nanoparticles show rapid overall elimination from the body

Finally, we studied the whole-body pharmacokinetics of intra-cisterna magna ^{111}In-AuNPs over 24 h (Fig. 6a). Rats were whole body SPECT scanned at 1.5 and 3 h under the initial ketamine-dexmedetomidine anesthesia that was used for surgery and otherwise
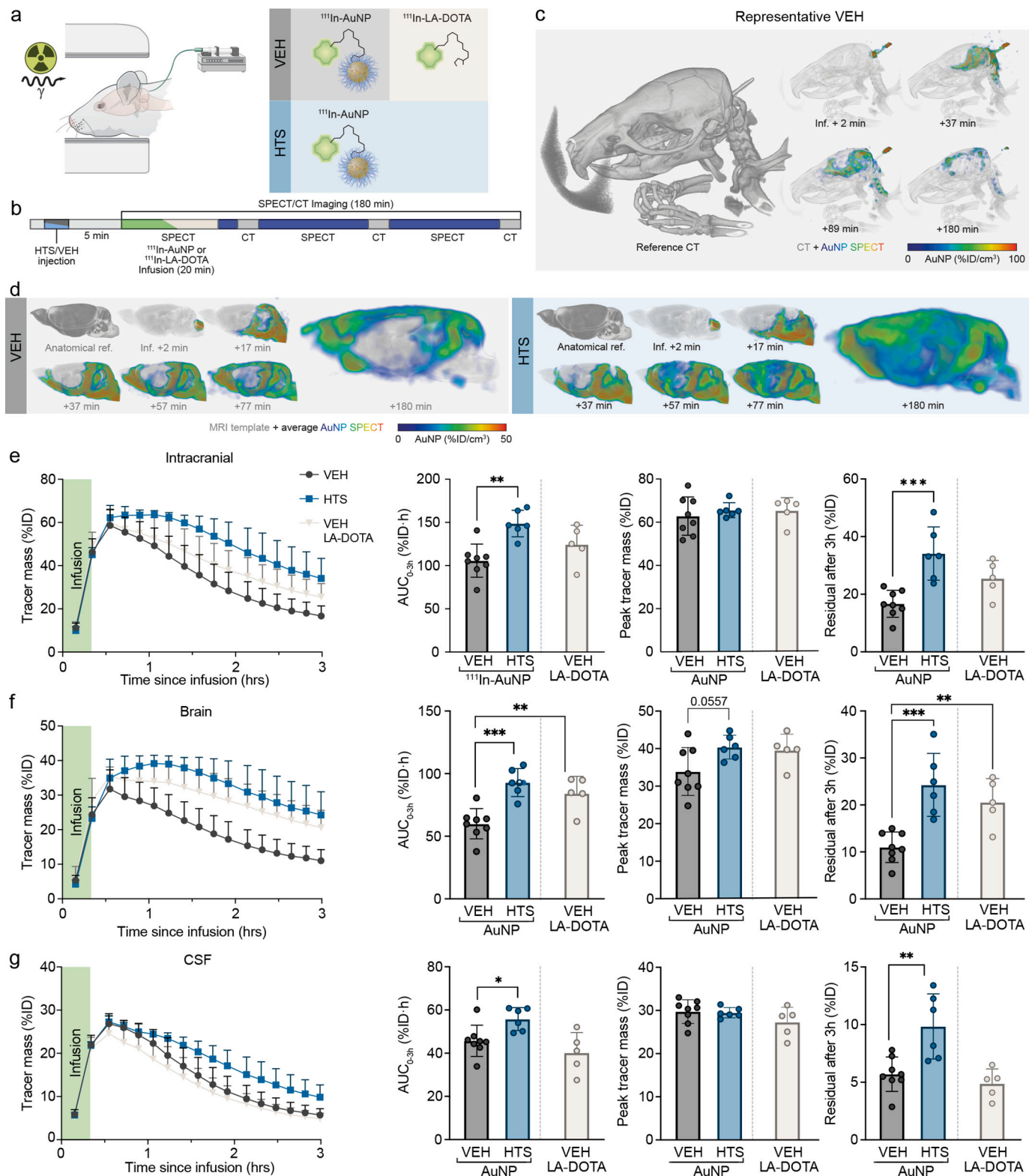
(caption on next page)

Fig. 2. Hypertonic saline treatment enhances the delivery of intrathecally infused small gold nanoparticles to the rat brain. a, Experimental setup used for SPECT imaging of the transport of ^{111}In-AuNP or ^{111}In-LA-DOTA infused to the cisterna magna of rats under ketamine/dexmedetomidine anesthesia. b, Experimental timeline. Rats received an intraperitoneal injection of either isotonic (VEH, n = 8) or hypertonic saline (HTS, n = 6). ^{111}In-AuNP dispersion was infused to the cisterna magna and 180 min of SPECT was acquired interspersed with CT sessions. A third group was given an isotonic intraperitoneal injection and an intracisternal infusion of ^{111}In-LA-DOTA (VEH LA-DOTA, n = 5). c, Three-dimensional rendering of ^{111}In-AuNP SPECT overlaid on a CT image of a representative rat brain in the VEH group shows the distribution of ^{111}In-AuNP along the glymphatic pathway [32]. d. Three-dimensional rendering of population-based average SPECT images after infusion of ^{111}In-AuNP overlaid on a T2-weighted MRI brain template. e, Intracranial exposure to ^{111}In-AuNPs increased by 40% and residual ^{111}In-AuNP content at three hours was doubled in the HTS group compared with VEH as demonstrated by the time-activity curve (left) and AUC$_{0-3h}$ (right) of ^{111}In-AuNP. f-g, Comparison of time-activity-curves (left) and AUCs (right) of ^{111}In-AuNP or ^{111}In-LA-DOTA after segmenting the intracranial compartment into brain (f) and CSF (g). AUC$_{0-3}$, area under the time-activity-curve (TAC) from 0 to 3 h; CT, computed tomography; HTS, hypertonic saline; ^{111}In-AuNPs, [111]indium-labelled gold nanoparticles; ^{111}In-LA-DOTA, [111]indium-labelled conjugate (lipoic acid–1,4,7,10-tetraazacyclododecane-1,4,7,10-tetraacetic acid); MRI, magnetic resonance imaging; SPECT, single-photon emission tomography; VEH: vehicle/control group; %ID: percent of the infused dose. *: $p < 0.05$, **: $p < 0.01$, ***: $p < 0.001$, ****: $p < 0.0001$. Error bars represent standard deviation. Quantitation and statistics are detailed in Supplementary Information S7. (For interpretation of the references to colour in this figure legend, the reader is referred to the web version of this article.)
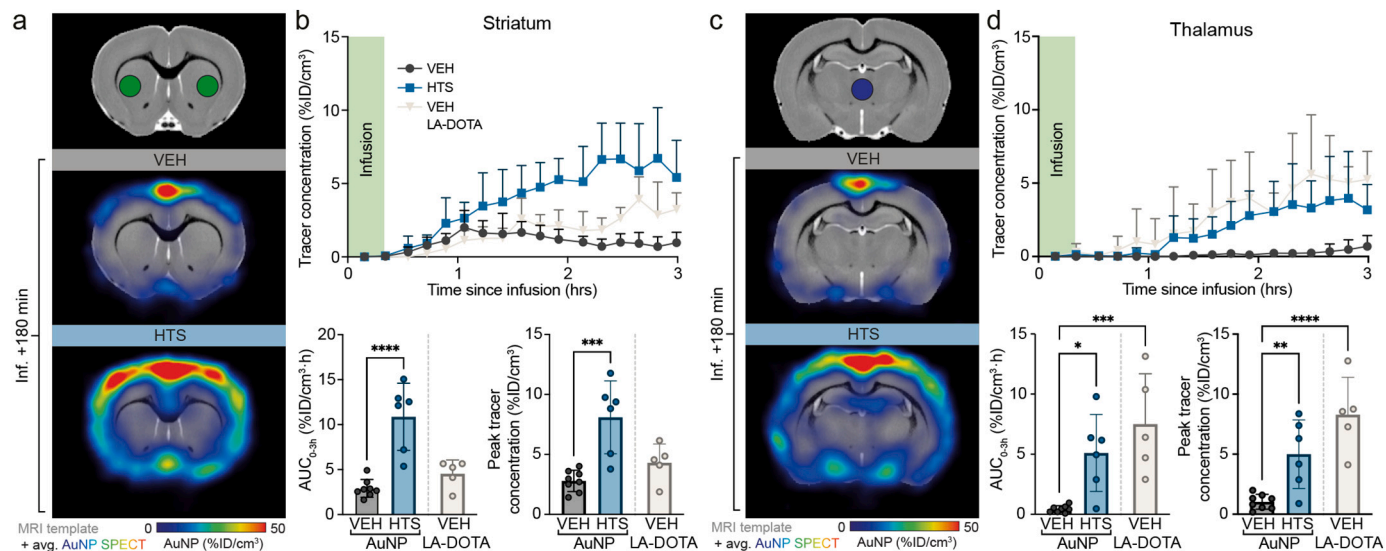

Fig. 3. Manyfold exposure to gold nanoparticles in deep brain regions by hypertonic saline treatment after intrathecal delivery. Rats received an intracisternal cannula and were placed in the SPECT scanner under ketamine/dexmedetomidine anesthesia. Five minutes prior to intracisternal infusion, rats received an intraperitoneal injection of either isotonic (VEH, $n = 8$) or hypertonic saline (HTS, $n = 6$). ^{111}In-AuNP dispersion was infused to the cisterna magna and a dynamic SPECT sequence lasting 180 min was acquired interspersed with CT. A third treatment group was given an intraperitoneal injection of isotonic saline and an intracisternal infusion of ^{111}In-LA-DOTA (VEH LA-DOTA, $n = 5$). The experimental protocol is described in detail in Fig. 2a-b. We analyzed radioactivity concentrations in deep in brain tissue to avoid spill-over of radioactivity from the subarachnoid space. a, Spherical regions of interest (ROI) (diameter 1.4 mm) was placed in the bilateral caudate putamen. Coronal slices of group-wise population-based average ^{111}In-AuNP images show the radioactivity distribution at 180 min after intracisternal infusion. b, Analysis of time-activity-curves from striatal ROIs show three-fold increases in exposure and peak concentration of ^{111}In-AuNPs. c, A ROI was placed at the intrathalamic junction. Coronal slices of group-wise population-based average ^{111}In-AuNP images show the tracer distribution at 180 min after infusion. d, Analysis of time-activity-curves from the thalamic ROIs show a ten-fold increase in exposure and five-fold increase in peak concentration of ^{111}In-AuNPs by HTS treatment. AUC$_{0-3h}$, area under the time-activity-curve from 0 to 3 h; HTS, hypertonic saline; ^{111}In-AuNPs, [111]indium-labelled gold nanoparticles; LA-DOTA, [111]indium-labelled conjugate (lipoic acid–1,4,7,10-tetraazacyclododecane-1,4,7,10-tetraacetic acid); MRI, magnetic resonance imaging; SPECT, single-photon emission tomography; VEH: vehicle/control group; %ID: percent of the infused dose. *: $p < 0.05$, **: $p < 0.01$, ***: $p < 0.001$, ****: $p < 0.0001$. Error bars represent standard deviation. Quantitation and statistics are detailed in Supplementary Information S7. (For interpretation of the references to colour in this figure legend, the reader is referred to the web version of this article.)

stayed in their home cage for recovery. For the SPECT scans at 4.5, 6, and 24 h post infusion, the rats were briefly anesthetized with isoflurane (1.5%). The decay-corrected sagittal (Fig. 6b-c) distribution profiles over 24 h showed relatively fast ^{111}In-AuNP clearance from the whole body. Gross distribution within the brain (Fig. 6d) resembled that in the earlier experiments focusing on the head and neck, with significantly higher whole-CNS (Fig. 6e) and intracranial (Fig. 6f) ^{111}In-AuNP exposure over 24 h (AUC$_{0-24h}$) in the HTS group compared with VEH. The dosimetry in the spinal canal (Fig. 6g) or whole-body AUC$_{0-24h}$ did not differ between groups (Fig. 6h). Whole-body time-activity-curves followed a biphasic elimination curve, divided into 1.5–4.5 h and 6–24 h after infusion. The biological half-life was significantly faster during the initial phase compared with the latter phase (VEH: 7.9 ± 2.9 h *vs* 18.1 ± 2.1 h, p < 0.0001; HTS: 10.1 ± 5.1 *vs.* 18.2 ± 1.8 h, $p = 0.01$), but did not differ between the treatment groups.

To assess the elimination of intracisternal ^{111}In-AuNPs from the body, we analyzed 24 h time-radioactivity curves in the kidney, bladder, lungs, and liver. Relatively high early activity in the kidney (Fig. 6i) and bladder (Fig. 6j) regions revealed renal excretion as a fast elimination route for ^{111}In-AuNPs infused to the cisterna magna. HTS significantly reduced the 24-h kidney exposure (AUC$_{0-24h}$), suggesting that clearance of ^{111}In-AuNPs from the CNS to general circulation was reduced by HTS. The lungs (Fig. 6k) and liver (Fig. 6l) showed only minor ^{111}In-AuNP exposure. Although the majority (approximately 95%) of ^{111}In-AuNPs had been cleared from the CNS at 24 h, there remained a small but significant group difference in the intracranial ^{111}In-AuNP distribution favoring the HTS group (Fig. 6m).

To visualize better the distribution of residual ^{111}In-AuNP-derived radioactivity in the body, we re-rendered the 24-h time point from Fig. 6d with 10-fold increased contrast (Fig. 6n). The majority of the
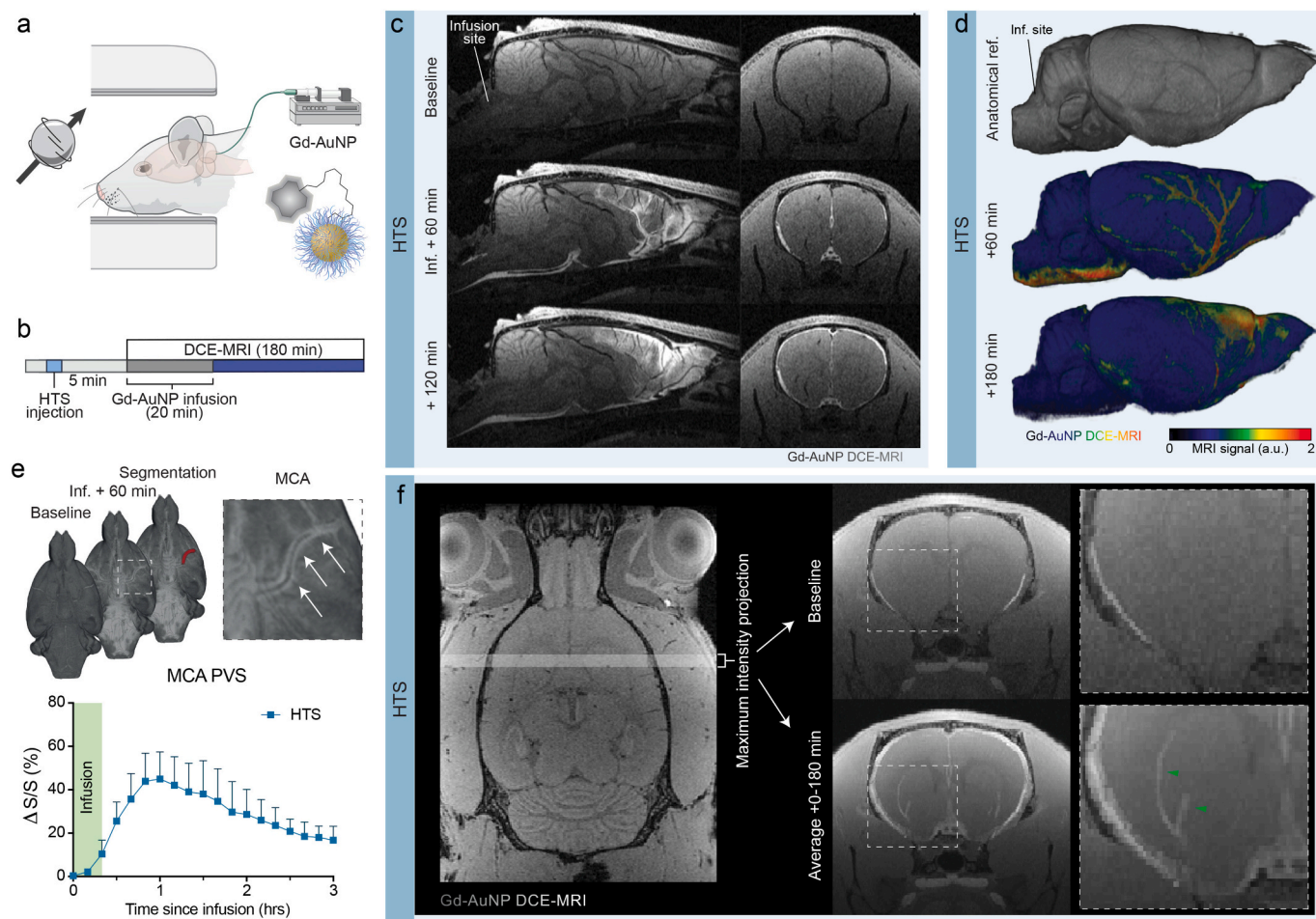
Fig. 4. Brain delivery of gadolinium-labelled small gold nanoparticles in the perivascular spaces of pial and penetrating arteries demonstrated with dynamic contrast-enhanced magnetic resonance imaging. a, Experimental setup used for DCE-MRI of the transport of Gd-AuNP infused to the cisterna magna of rats after hypertonic saline (HTS) treatment. b, Experimental timeline. Rats anesthetized with ketamine-dexmedetomidine were given an intraperitoneal injection of hypertonic saline (HTS, $n = 5$), and five minutes later, the Gd-AuNP dispersion was infused to the cisterna magna, with a DCE-MRI acquisition lasting 180 min. c, Representative sagittal and coronal slices from one rat shows the signal increase, mostly in periarterial spaces, caused by shortened T1 relaxation-time in the presence of paramagnetic gadolinium. d. Representative three-dimensional rendering in false colour shows the distribution of Gd-AuNPs across the perivascular network of the middle cerebral artery at 60 min, with most of the particles distributed across the subarachnoid space and brain at 180 min. e. Quantification of Gd-AuNP as percentage signal increase in the perivascular space of the middle cerebral artery shows that the concentration peaks 50 min after the beginning of the infusion and had declined by two thirds at 180 min. f. To increase sensitivity to the Gd-AuNP signal, we averaged all DCE-MRI frames from before (baseline) and after infusion (avg. 0–180 min) and created a maximum-intensity projection of the delineated region (left). Post-infusion signal enhancement is clearly seen in deep striatal perivascular spaces (green arrows). Gd-AuNP, gadolinium-labelled gold nanoparticle; DCE-MRI, dynamic contrast-enhanced magnetic resonance imaging; HTS, hypertonic saline; Inf., infusion; MCA, middle cerebral artery; PVS, perivascular space; ref., reference. Error bars represent standard deviation. (For interpretation of the references to colour in this figure legend, the reader is referred to the web version of this article.)

remaining radioactivity in the brain was in close vicinity to the superior sagittal sinus and the transverse sinuses, in agreement with a previous study reporting the accumulation of large-molecular weight particles near dural venous sinuses after intrathecal administration was reported [38]. In conclusion, clearance of intracisternally administered small ^{111}In-AuNPs from the whole body was rapid, with 69% of total radioactivity cleared from the body at 24 h in the VEH group *versus* 66% in the HTS group ($p = 0.28$).

4. Discussion

In this study, we report a strategy for brain-wide drug delivery *via* nanoparticles. We chose to study small AuNPs for three reasons: first, they are expected to retain their size and shape *in vivo* [39], second, they are of small diameter which we anticipated would enable their access through the periarterial space into the brain parenchyma as has been previously described [8,40], and third, they can be renally excreted after

their egress from the CNS [41]. After intrathecal administration, the small AuNPs distributed widely in the CSF space. Transient enhancement of periarterial glymphatic flow by systemic HTS enhanced the brain delivery of AuNPs and markedly improved the penetration of AuNPs into the deep brain structures, as demonstrated by the 3.7- and 12-fold AUC_{0-3h} increases in the striatum and thalamus, respectively. Although nearly all of the AuNPs had been cleared from the CNS at 24 h, there persisted a small but significant concentration difference favoring the hypertonic treatment group. Our findings suggest that facilitating perivascular glymphatic influx by hypertonic saline administration is an effective strategy for delivering small nanoparticles into deep brain regions using a relatively non-invasive and safe approach.

Previous studies of the biodistribution of intrathecally administered nanoparticles have mainly employed using *ex vivo* techniques and larger nanoparticles. Our dynamic *in vivo* SPECT and MRI imaging approaches overcome the limitations of *ex vivo* methods, such as the requirement for perfusion fixation and euthanasia, which causes a rapid marked
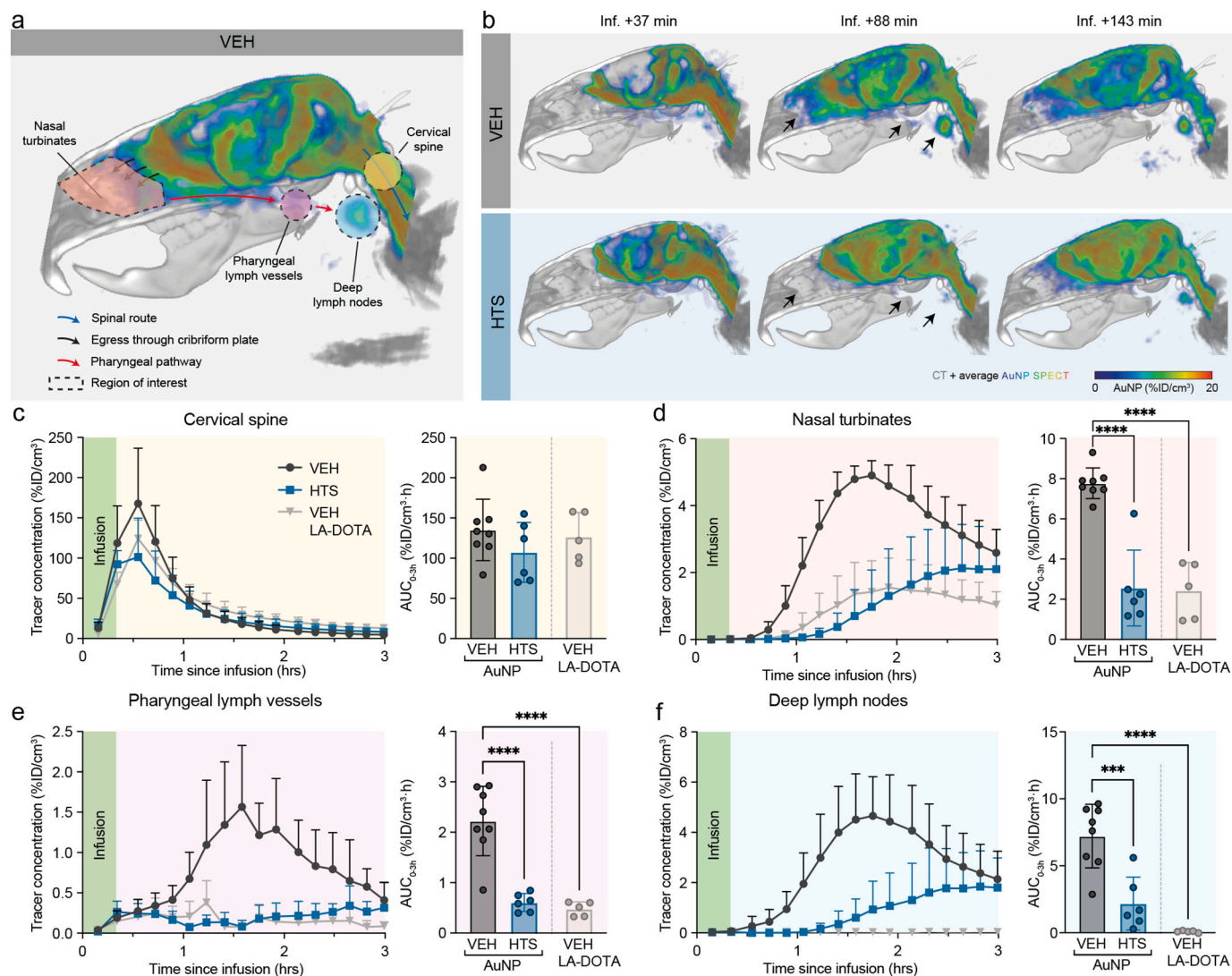
Fig. 5. Decreased egress of small gold nanoparticles to the lymphatic structures of the rat head and neck after hypertonic saline treatment. a, Three-dimensional rendering of vehicle-group average (VEH, $n = 8$) ^{111}In-AuNP SPECT overlaid on a CT template shows visible efflux routes from the intracranial compartment. Efflux routes include caudal-directed flow in the subarachnoid space of the spinal canal and the rostral egress through the cribriform plate and nasal turbinates towards the deep cervical lymph nodes. ROIs for quantification of ^{111}In-AuNP exposure are illustrated with dashed lines. b, Comparison between average SPECT from VEH (n = 8) and HTS ($n = 6$) groups shows that efflux through nasal route and to deep lymph nodes appears reduced or delayed with HTS treatment. c, No significant difference in ^{111}In-AuNP exposure (AUC) between HTS and VEH groups was seen in the cervical spine, whereas AuNP exposure was significantly reduced with HTS treatment in nasal turbinates (d), pharyngeal lymph structures (e), and deep lymph nodes (f). In contrast, the availability of the low-molecular ^{111}In-LA-DOTA conjugate was significantly reduced in nasal turbinates (d) and pharyngeal lymph structures (e), and was virtually abolished in deep lymph nodes (f). AUC$_{0-3h}$, area under the time-activity-curve from 0 to 3 h; CT, computed tomography; HTS, hypertonic saline; Inf., infusion; ^{111}In-AuNP, [111]indium-labelled gold nanoparticle; VEH, vehicle/control group, ***: $p < 0.001$, ****: $p < 0.0001$. Error bars represent standard deviation. Quantitation and statistics are detailed in Supplementary Information S7. (For interpretation of the references to colour in this figure legend, the reader is referred to the web version of this article.)

perivascular CSF influx [42,43]. This would likely have led to over-estimating the parenchymal distribution of tracers. The nanoparticles used in previous reports *ex vivo* have been ten times larger than the 10–15 nm AuNPs in this study. Householder and colleagues administered 122 nm diameter PEGylated polystyrene nanoparticles into the cisterna magna of mice and observed their widespread distribution in the subarachnoid space but no entry into deeper brain structures [44]. Likewise, Dengler et al. reported no deep brain distribution for mesoporous silica nanoparticles measuring 230 nm in diameter [45]. Two studies have reported on nanoparticle-mediated delivery of siRNA into the brain parenchyma, albeit without quantifying the accumulation of nanoparticles [46,47]. Thus, the literature suggests that parenchymal entry of intrathecally administered large nanoparticles does not occur to a significant extent.

Our strategy here was to administer small AuNPs concomitantly with

HTS, thus exploiting the finding that systemic HTS transiently boosts glymphatic delivery of IgG-sized (maximum diameter of 14.5 nm [48]) antibodies [14]. We administered 40 mOsm kg^{-1} of HTS, a dose that is within the order of magnitude that is routinely used in clinical trials and practice [49]. Surprisingly, the effect of HTS compared with the isotonic group persisted in brain at 24 h, suggesting that HTS influences drug availability longer than its effect on intracranial pressure, which may last four to five hours in humans [50,51]. HTS has been used in various clinical contexts, most often to treat elevated intracranial pressure or to restore blood pressure in patients with shock [49]. Despite marked elevations in plasma osmolality or sodium levels, these trials have not reported serious adverse effects related to the use of HTS [50]. The most severe potential adverse effect reported is central pontine myelinolysis, which may be a particular threat in malnourished or hyponatremic individuals, whose sodium level is corrected too rapidly [50]. In healthy
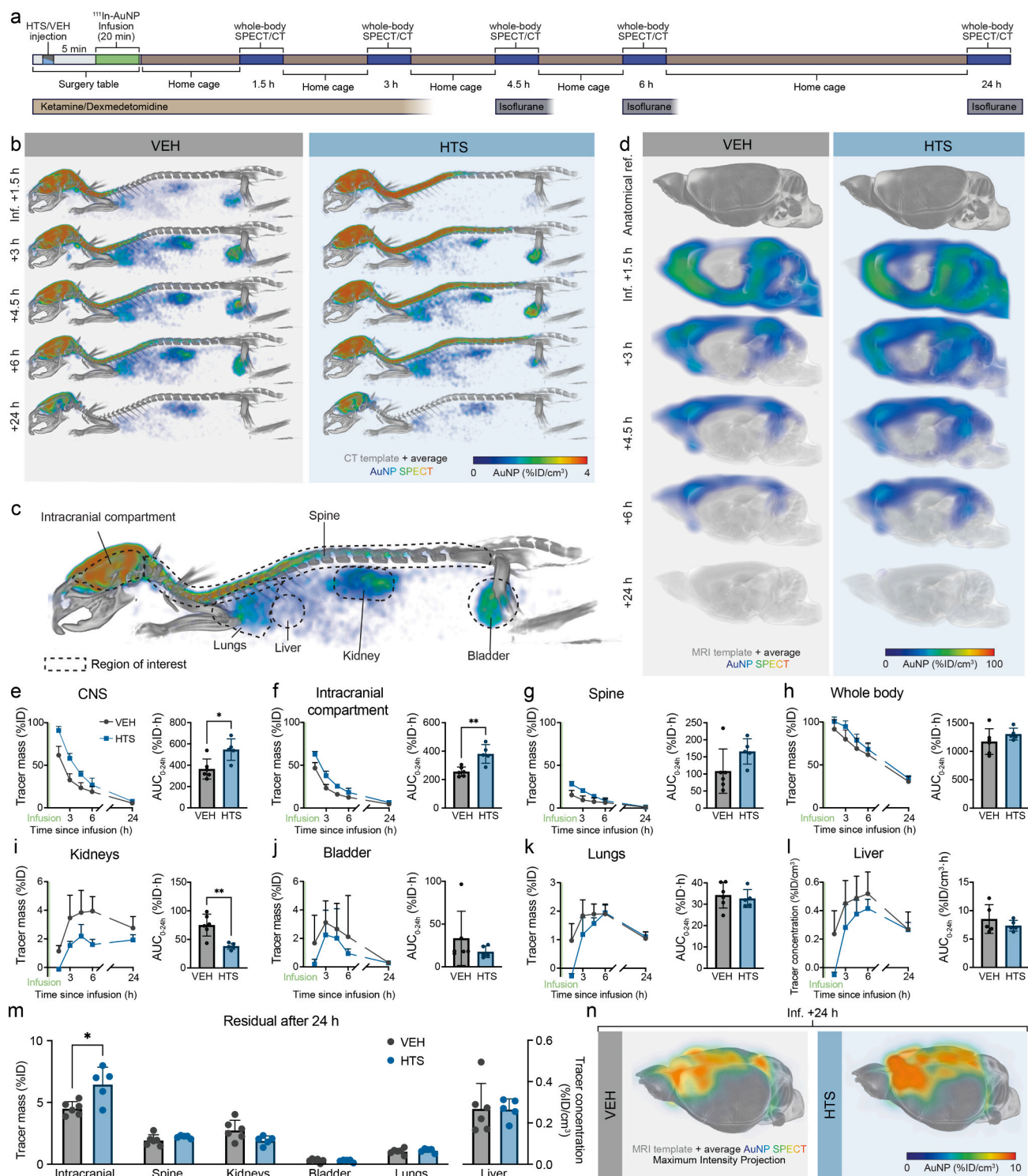
Fig. 6. Whole-body elimination of intrathecally administered ^{111}In-labelled gold nanoparticles. a, Experimental timeline. Rats were anesthetized with ketamine/dexmedetomidine and given an intraperitoneal injection of either isotonic (VEH, $n = 6$) or hypertonic saline (HTS, $n = 5$). After subsequent infusion of ^{111}In-AuNP dispersion into the cisterna magna, rats were returned to their home cage, and full-body SPECT and CT were acquired at 1.5, 3, 4.5, 6 and 24 h after infusion. Between 3 and 4.5 h, the rats recovered from initial anesthesia, and they were briefly re-anesthetized with isoflurane (1.5%) for subsequent SPECT scans. b, Whole-body population-based average SPECT images after infusion of ^{111}In-AuNP overlaid on a full body CT template. c, Illustration of regions of interest. d, Three-dimensional renderings of population-based average SPECT images after infusion of ^{111}In-AuNP overlaid on a T2-weighted MRI brain template. e-l, Comparisons of time-activity-curves of ^{111}In-AuNP in regions of interest. m, Residual ^{111}In-AuNP mass or concentration at 24 h in organs of interest. n, Residual ^{111}In-AuNP distribution at 24 h depicted with a maximum intensity projection overlaid on an MRI template. The 24-h time point has been shown with tenfold increased contrast compared with d. AUC$_{0-24h}$: area under the time-activity-curve between 0 and 24 h; HTS, hypertonic saline; ^{111}In-AuNP, [111]Indium-labelled gold nanoparticle; VEH: vehicle/control group *: $p < 0.05$, **: $p < 0.01$, ****: $p < 0.0001$. Quantitation and statistics are detailed in Supplementary Information S7. (For interpretation of the references to colour in this figure legend, the reader is referred to the web version of this article.)

volunteers, intravenous infusion of 10 mOsm kg^{-1} of HTS over 30 min led to a rapid increase in plasma volume and elevated serum sodium levels, with no reported adverse effects [52]. Thus, the systemic hypertonic intervention is a clinically available and safe intervention that should be further investigated as an adjunct to intrathecally administered therapeutics in CNS drug delivery.

Another advantage of our present approach was the use of an optimized anesthetic regimen. We chose to use a combination of ketamine and the α₂-adrenergic agonist dexmedetomidine, as such a mixture is known to improve glymphatic uptake of tracers into the rodent brain [11–13]. Further, the high α₂-receptor selectivity and slow-wave inducing properties of dexmedetomidine should theoretically be superior to the previously used ketamine-xylazine anesthesia, which represents another frequently used anesthetic regimen that can increase glymphatic CSF influx compared to volatile anesthetics or the awake state [10,13,35]. Additionally, unlike xylazine, both ketamine and dexmedetomidine are widely used in procedural and intensive care sedation in humans, making this anesthetic regimen potentially applicable in the clinic.

Tailored AuNPs could be used to deliver a variety of high-molecular weight drugs relevant for treating diseases affecting the CNS. In general, AuNPs can be surface-functionalized through carboxylates or the formation of Au—S bonds, which are known to exhibit considerable stability *in vivo* [53]. Accordingly, pharmacologically active compounds can be attached directly to the AuNP surface, or conjugated *via* other substances, such as PEG-thiol polymers or lipoic acid, which are in turn covalently bound to the AuNP surface. Such modifications have been used to prepare AuNPs decorated with antibodies for receptor targeting [53,54], oligonucleotides for gene silencing [55], and release systems for low-molecular weight drugs [53]. These various possibilities for modification possibilities make AuNPs highly relevant for a variety of therapies, currently hindered by poor access of medications to the brain.

Due to the extensive network of perivascular spaces in the brain, we expect the glymphatic-enhanced AuNP brain delivery strategies to prove particularly valuable in the treatment of diffuse diseases affecting the brain, such as brain cancers without clear margins or in neurodegenerative diseases. Indeed, nanoparticles may be particularly useful in brain cancer as they can be readily modified to function as theranostic agents with the dual function of imaging and therapy [4], and potentially overcome antineoplastic drug resistance [56]. As a relatively non-selective transport route, it seems highly likely that glymphatic-enhanced transport could be harnessed for the delivery of both simple, non-targeted nanoparticles, and likewise more intricate functionalized nanoparticle designs. In addition, as our study was designed with particle size in mind, we expect glymphatic delivery to be operational for other nanoparticle types in a similar size range. In particular, this includes biocompatible polymer-based nanoparticles, which can be synthetically modified in diverse ways to carry therapeutic substances and target cancer cell structures, thereby greatly expanding the scope of this therapeutic approach.

We surmise that our approach for circumventing the BBB through intrathecal administration is inherently superior to systemic chemotherapy targeting the whole brain, as the exclusion of many substances from brain [4,57,58] may call for excessive doses causing systemic adverse effects. Intrathecal administration of therapeutics is extensively used in clinical practice, for instance in pain management [59], antimicrobial administration [60], and chemotherapy [61]. The lumbar intrathecal route is the most frequently used technique, and is generally safe according to a large survey from Sweden that reported a complications rate of 1 per 20–30,000 after intrathecal anesthesia [62]. Due to the potentially low brain exposure after lumbar injection, recent delivery research has also focused on the more invasive intracisternal delivery, as in the current preclinical study. While intracisternal administration may certainly require radiological or surgical techniques, it could lead to significantly greater drug concentrations in the brain [63]. Due to the general difficulty of overcoming the BBB, we

anticipate that intrathecal drug administration route will assume a markedly increased clinical role.

There are several directions for future studies regarding glymphatic-assisted AuNP delivery to the CNS. First, the effects of HTS on glymphatic efflux have only been little addressed. Recent results show that while HTS is an efficient driver of CSF influx to the brain parenchyma, its effect on brain clearance of intrastriatally infused ^{99m}Tc-DTPA is negligible [15]. Our results showing modest clearance of AuNPs from the CNS (Fig. 6e–g) are in line with these findings, suggesting that HTS could be a very efficient tool in delivering and retaining drugs in the brain. However, more research with different tracer molecules and infusion sites are needed to fully characterize effects on glymphatic efflux. Second, while the present SPECT and MRI allow the tracking of AuNPs to deep brain regions *in vivo*, these methods do not allow assessing the fate of the AuNPs at the cellular level. Our study is pharmacokinetics-focused without a disease model and more *in vivo* studies with a biological reporter confirming exact localization and target binding are needed. Finally, some *in vitro* assays [64] have suggested toxicity of AuNPs at high concentrations. Our study did not thoroughly assess the toxicity of intrathecal AuNPs, but the 24-h experiment performed in awake animals suggested no directly observable adverse effects. The possible CNS toxicity of AuNPs need to be assessed in further *in vivo* trials.

5. Conclusion

Here, we demonstrate that the brain-wide availability of intrathecally administered small gold nanoparticles can be enhanced by systemic hypertonic saline, with effects lasting up to 24 h *in vivo*. Further, the nanoparticles were rapidly eliminated from the body after leaving the CNS, this obviating concerns about renal toxicity. As the astrocytic gaps in the endfeet are most likely a significant limiting factor for drug delivery to the neuropil [8,40], we suppose that nanoparticles of different sizes could be used experimentally to assess indirectly the astrocytic gap width *in vivo*. Future studies should characterize the optimal size and properties of nanoparticles for glymphatic intrathecal delivery. As systemic hypertonic saline treatment has been studied in healthy volunteers and is already in clinical use, the stage is set for clinical trials to assess glymphatic-assisted drug delivery with intrathecal therapeutics.

CRediT authorship contribution statement

Tuomas O. Lilius: Conceptualization, Methodology, Validation, Investigation, Resources, Writing – original draft, Visualization, Supervision, Project administration, Funding acquisition. **Kristian Nygaard Mortensen:** Conceptualization, Methodology, Software, Validation, Formal analysis, Investigation, Resources, Data curation, Writing – original draft, Visualization, Project administration. **Claire Deville:** Methodology, Validation, Formal analysis, Investigation, Writing – original draft, Visualization. **Terhi J. Lohela:** Validation, Writing – original draft. **Frederik Filip Stæger:** Formal analysis, Investigation, Writing – review & editing. **Björn Sigurdsson:** Formal analysis, Investigation, Writing – review & editing. **Elisabetta M. Fiordaliso:** Investigation, Writing – review & editing. **Marko Rosenholm:** Investigation, Writing – review & editing. **Chris Kamphuis:** Software, Validation, Writing – review & editing. **Freek J. Beekman:** Software, Validation, Writing – review & editing. **Andreas I. Jensen:** Conceptualization, Methodology, Validation, Investigation, Resources, Writing – original draft, Visualization, Supervision, Project administration, Funding acquisition. **Maiken Nedergaard:** Conceptualization, Methodology, Resources, Writing – review & editing, Supervision, Funding acquisition.

Declaration of Competing Interest

The authors declare no competing interests.

Data availability

The authors declare that the main data supporting the findings of this study are available within the article and its Supplementary Information files. Extra data are available from the corresponding author upon request.

Acknowledgements

Appendix A. Supplementary data

Supplementary data to this article can be found online at https://doi.org/10.1016/j.jconrel.2023.01.054.

References

[1] GBD, Neurology collaborators, global, regional, and national burden of neurological disorders, 1990-2016: a systematic analysis for the global burden of disease study 2016, Lancet Neurol. 18 (2019) (2016) 459–480, https://doi.org/10.1016/S1474-4422(18)30499-X.

[2] M.J. Fowler, J.D. Cotter, B.E. Knight, E.M. Sevick-Muraca, D.I. Sandberg, R. W. Sirianni, Intrathecal drug delivery in the era of nanomedicine, Adv. Drug Deliv. Rev. (2020), https://doi.org/10.1016/j.addr.2020.02.006.

[3] M.J. Mitchell, M.M. Billingsley, R.M. Haley, M.E. Wechsler, N.A. Peppas, R. Langer, Engineering precision nanoparticles for drug delivery, Nat. Rev. Drug Discov. 20 (2021) 101–124, https://doi.org/10.1038/s41573-020-0090-8.

[4] W. Tang, W. Fan, J. Lau, L. Deng, Z. Shen, X. Chen, Emerging blood-brain-barrier-crossing nanotechnology for brain cancer theranostics, Chem. Soc. Rev. 48 (2019) 2967–3014, https://doi.org/10.1039/c8cs00805a.

[5] K. Park, Optimal nanoparticle design for effective transport through the blood-brain barrier, J. Control. Release 295 (2019) 290, https://doi.org/10.1016/j.jconrel.2019.01.024.

[6] D.J. Wolak, R.G. Thorne, Diffusion of macromolecules in the brain: implications for drug delivery, Mol. Pharm. 10 (2013) 1492–1504, https://doi.org/10.1021/mp300495e.

[7] T.J. Lohela, T.O. Lilius, M. Nedergaard, The glymphatic system: implications for drugs for central nervous system diseases, Nat. Rev. Drug Discov. 21 (2022) 763–779, https://doi.org/10.1038/s41573-022-00500-9.

[8] J.J. Iliff, M. Wang, Y. Liao, B.A. Plogg, W. Peng, G.A. Gundersen, et al., A paravascular pathway facilitates CSF flow through the brain parenchyma and the clearance of interstitial solutes, including amyloid β, Sci. Transl. Med. 4 (2012) 147ra111, https://doi.org/10.1126/scitranslmed.3003748.

[9] M. Nedergaard, Neuroscience. Garbage truck of the brain, Science. 340 (2013) 1529–1530, https://doi.org/10.1126/science.1240514.

[10] L. Xie, H. Kang, Q. Xu, M.J. Chen, Y. Liao, M. Thiyagarajan, et al., Sleep drives metabolite clearance from the adult brain, Science. 342 (2013) 373–377, https://doi.org/10.1126/science.1241224.

[11] H. Benveniste, H. Lee, F. Ding, Q. Sun, E. Al-Bizri, R. Makaryus, et al., Anesthesia with Dexmedetomidine and low-dose isoflurane increases solute transport via the Glymphatic pathway in rat brain when compared with high-dose isoflurane, Anesthesiology. 127 (2017) 976–988, https://doi.org/10.1097/ALN.0000000000001888.

[12] T.O. Lilius, K. Blomqvist, N.L. Hauglund, G. Liu, F.F. Stæger, S. Bærentzen, et al., Dexmedetomidine enhances glymphatic brain delivery of intrathecally administered drugs, J. Control. Release 304 (2019) 29–38, https://doi.org/10.1016/j.jconrel.2019.05.005.

[13] L.M. Hablitz, H.S. Vinitsky, Q. Sun, F.F. Stæger, B. Sigurdsson, K.N. Mortensen, et al., Increased glymphatic influx is correlated with high EEG delta power and low heart rate in mice under anesthesia, Sci. Adv. 5 (2019) eaav5447.

[14] B.A. Plog, H. Mestre, G.E. Olveda, A.M. Sweeney, H.M. Kenney, A. Cove, et al., Transcranial optical imaging reveals a pathway for optimizing the delivery of immunotherapeutics to the brain, JCI Insight. 3 (2018) 1188, https://doi.org/10.1172/jci.insight.120922.

[15] T.O. Lilius, M. Rosenholm, L. Klinger, K.N. Mortensen, B. Sigurdsson, F.L.-H. Mogensen, et al., SPECT/CT imaging reveals CNS-wide modulation of glymphatic cerebrospinal fluid flow by systemic hypertonic saline, iScience 25 (2022), 105250, https://doi.org/10.1016/j.isci.2022.105250.

[16] K.J. Blomqvist, M.O.B. Skogster, M.J. Kurkela, M.P. Rosenholm, F.H.G. Ahlström, M.T. Airavaara, et al., Systemic hypertonic saline enhances glymphatic spinal cord delivery of lumbar intrathecal morphine, J. Control. Release 344 (2022) 214–224, https://doi.org/10.1016/j.jconrel.2022.03.022.

[17] J.C. McGrath, G.B. Drummond, E.M. McLachlan, C. Kilkenny, C.L. Wainwright, Guidelines for reporting experiments involving animals: the ARRIVE guidelines, Br. J. Pharmacol. 160 (2010) 1573–1576, https://doi.org/10.1111/j.1476-5381.2010.00873.x.

[18] J. Piella, N.G. Bastús, V. Puntes, Size-controlled synthesis of Sub-10-nanometer citrate-stabilized gold nanoparticles and related optical properties, Chem. Mater. 28 (2016) 1066–1075, https://doi.org/10.1021/acs.chemmater.5b04406.

[19] A.F. Frellsen, A.E. Hansen, R.I. Jølck, P.J. Kempen, G.W. Severin, P.H. Rasmussen, et al., Mouse positron emission tomography study of the biodistribution of gold nanoparticles with different surface coatings using embedded Copper-64, ACS Nano 10 (2016) 9887–9898, https://doi.org/10.1021/acsnano.6b03144.

[20] J.W. Seo, L.M. Mahakian, A. Kheirolomoom, H. Zhang, C.F. Meares, R. Ferdani, et al., Liposomal Cu-64 labeling method using bifunctional chelators: poly(ethylene glycol) spacer and chelator effects, Bioconjug. Chem. 21 (2010) 1206–1215, https://doi.org/10.1021/bc100018n.

[21] A.L.R. Xavier, N.L. Hauglund, S. von Holstein-Rathlou, Q. Li, S. Sanggaard, N. Lou, et al., Cannula implantation into the cisterna magna of rodents, J. Vis. Exp. (2018) e57378, https://doi.org/10.3791/57378.

[22] P.E.B. Vaissier, F.J. Beekman, M.C. Goorden, Similarity-regulation of OS-EM for accelerated SPECT reconstruction, Phys. Med. Biol. 61 (2016) 4300–4315, https://doi.org/10.1088/0031-9155/61/11/4300.

[23] M.C. Goorden, J. van Roosmalen, F. van der Have, F.J. Beekman, Optimizing modelling in iterative image reconstruction for preclinical pinhole PET, Phys. Med. Biol. 61 (2016) 3712–3733, https://doi.org/10.1088/0031-9155/61/10/3712.

[24] S. Jan, G. Santin, D. Strul, S. Staelens, K. Assie, D. Autret, et al., GATE: a simulation toolkit for PET and SPECT, Phys. Med. Biol. 49 (2004) 4543–4561, https://doi.org/10.1088/0031-9155/49/19/007.

[25] B.B. Avants, N.J. Tustison, G. Song, P.A. Cook, A. Klein, J.C. Gee, A reproducible evaluation of ANTs similarity metric performance in brain image registration, Neuroimage. 54 (2011) 2033–2044, https://doi.org/10.1016/j.neuroimage.2010.09.025.

[26] N.J. Tustison, B.B. Avants, P.A. Cook, Y. Zheng, A. Egan, P.A. Yushkevich, et al., N4ITK: improved N3 bias correction, IEEE Trans. Med. Imaging 29 (2010) 1310–1320, https://doi.org/10.1109/TMI.2010.2046908.

[27] B.B. Avants, N.J. Tustison, J. Wu, P.A. Cook, J.C. Gee, An open source multivariate framework for n-tissue segmentation with evaluation on public data, Neuroinformatics. 9 (2011) 381–400, https://doi.org/10.1007/s12021-011-9109-y.

[28] A. Sartori, F. Bianchini, S. Migliari, P. Burreddu, C. Curti, F. Vacondio, et al., Synthesis and preclinical evaluation of a novel, selective in-111-labelled aminoproline-RGD-peptide for non-invasive melanoma tumor imaging, Medchemcomm. 6 (2015) 2175–2183, https://doi.org/10.1039/c5md00301f.

[29] A.D. Sherry, P. Caravan, R.E. Lenkinski, Primer on gadolinium chemistry, J. Magn. Reson. Imaging 30 (2009) 1240–1248, https://doi.org/10.1002/jmri.21966.

[30] A. Laznickova, M. Petrik, P. Hermann, I. Lukes, Labeling of a bifunctional monophosphinic acid DOTA analogue with in-111: radiochemical aspects and preclinical results, J. Radioanal. Nucl. Chem. 273 (2007) 583–586, https://doi.org/10.1007/s10967-007-0914-6.

[31] G. Carlucci, H.J.K. Ananias, Z. Yu, H.D. Hoving, W. Helfrich, R.A.J.O. Dierckx, et al., Preclinical evaluation of a novel ^{111}In-labeled bombesin homodimer for improved imaging of GRPR-positive prostate cancer, Mol. Pharm. 10 (2013) 1716–1724, https://doi.org/10.1021/mp3005462.

[32] J.J. Iliff, H. Lee, M. Yu, T. Feng, J. Logan, M. Nedergaard, et al., Brain-wide pathway for waste clearance captured by contrast-enhanced MRI, J. Clin. Invest. 123 (2013) 1299–1309, https://doi.org/10.1172/JCI67677.

[33] L. Yang, B.T. Kress, H.J. Weber, M. Thiyagarajan, B. Wang, R. Deane, et al., Evaluating glymphatic pathway function utilizing clinically relevant intrathecal infusion of CSF tracer, J. Transl. Med. 11 (2013) 107, https://doi.org/10.1186/1479-5876-11-107.

[34] S.T. Proulx, Cerebrospinal fluid outflow: a review of the historical and contemporary evidence for arachnoid villi, perineural routes, and dural lymphatics, Cell. Mol. Life Sci. 78 (2021) 2429–2457, https://doi.org/10.1007/s00018-020-03706-5.

[35] E.H. Stanton, N.D.Å. Persson, R.S. Gomolka, T. Lilius, B. Sigurðsson, H. Lee, et al., Mapping of CSF transport using high spatiotemporal resolution dynamic contrast-enhanced MRI in mice: effect of anesthesia, Magn. Reson. Med. 85 (2021) 3326–3342, https://doi.org/10.1002/mrm.28645.

[36] M.W. Bradbury, R.J. Westrop, Factors influencing exit of substances from cerebrospinal fluid into deep cervical lymph of the rabbit, J. Physiol. Lond. 339 (1983) 519–534, https://doi.org/10.1113/jphysiol.1983.sp014731.

[37] J.H. Ahn, H. Cho, J.-H. Kim, S.H. Kim, J.-S. Ham, I. Park, et al., Meningeal lymphatic vessels at the skull base drain cerebrospinal fluid, Nature. 572 (2019) 62–66, https://doi.org/10.1038/s41586-019-1419-5.

[38] A. Louveau, J. Herz, M.N. Alme, A.F. Salvador, M.Q. Dong, K.E. Viar, et al., CNS lymphatic drainage and neuroinflammation are regulated by meningeal lymphatic vasculature, Nat. Neurosci. 21 (2018) 1380–1391, https://doi.org/10.1038/s41593-018-0227-9.

[39] A.M. Alkilany, S.E. Lohse, C.J. Murphy, The gold standard: gold nanoparticle libraries to understand the nano-bio interface, Acc. Chem. Res. 46 (2013) 650–661, https://doi.org/10.1021/ar300015b.

[40] M.E. Pizzo, D.J. Wolak, N.N. Kumar, E. Brunette, C.L. Brunnquell, M.-J. Hannocks, et al., Intrathecal antibody distribution in the rat brain: surface diffusion,

perivascular transport and osmotic enhancement of delivery, J. Physiol. Lond. 596 (2018) 445–475, https://doi.org/10.1113/JP275105.

[41] M. Longmire, P.L. Choyke, H. Kobayashi, Clearance properties of nano-sized particles and molecules as imaging agents: considerations and caveats, Nanomedicine (Lond). 3 (2008) 703–717, https://doi.org/10.2217/17435889.3.5.703.

[42] Q. Ma, M. Ries, Y. Decker, A. Müller, C. Riner, A. Bücker, et al., Rapid lymphatic efflux limits cerebrospinal fluid flow to the brain, Acta Neuropathol. 137 (2019) 151–165, https://doi.org/10.1007/s00401-018-1916-x.

[43] T. Du, H. Mestre, B.T. Kress, G. Liu, A.M. Sweeney, A.J. Samson, et al., Cerebrospinal fluid is a significant fluid source for anoxic cerebral oedema, Brain. (2021), https://doi.org/10.1093/brain/awab293.

[44] K.T. Householder, S. Dharmaraj, D.I. Sandberg, R.J. Wechsler-Reya, R.W. Sirianni, Fate of nanoparticles in the central nervous system after intrathecal injection in healthy mice, Sci. Rep. 9 (2019) 12587–12512611, https://doi.org/10.1038/s41598-019-49028-w.

[45] E.C. Dengler, J. Liu, A. Kerwin, S. Torres, C.M. Olcott, B.N. Bowman, et al., Mesoporous silica-supported lipid bilayers (protocells) for DNA cargo delivery to the spinal cord, J. Control. Release 168 (2013) 209–224, https://doi.org/10.1016/j.jconrel.2013.03.009.

[46] R. Shyam, Y. Ren, J. Lee, K.E. Braunstein, H.-Q. Mao, P.C. Wong, Intraventricular delivery of siRNA nanoparticles to the central nervous system, Mol Ther Nucleic Acids. 4 (2015), e242, https://doi.org/10.1038/mtna.2015.15.

[47] Y. Hagihara, Y. Saitoh, Y. Kaneda, E. Kohmura, T. Yoshimine, Widespread gene transfection into the central nervous system of primates, Gene Ther. 7 (2000) 759–763, https://doi.org/10.1038/sj.gt.3301169.

[48] Y.H. Tan, M. Liu, B. Nolting, J.G. Go, J. Gervay-Hague, G.-Y. Liu, A nanoengineering approach for investigation and regulation of protein immobilization, ACS Nano 2 (2008) 2374–2384, https://doi.org/10.1021/nn800508f.

[49] G.F. Strandvik, Hypertonic saline in critical care: a review of the literature and guidelines for use in hypotensive states and raised intracranial pressure, Anaesthesia. 64 (2009) 990–1003, https://doi.org/10.1111/j.1365-2044.2009.05986.x.

[50] J. Shi, L. Tan, J. Ye, L. Hu, Hypertonic saline and mannitol in patients with traumatic brain injury: a systematic and meta-analysis, Medicine (Baltimore) 99 (2020), e21655, https://doi.org/10.1097/MD.0000000000021655.

[51] N. Sakellaridis, E. Pavlou, S. Karatzas, D. Chroni, K. Vlachos, K. Chatzopoulos, et al., Comparison of mannitol and hypertonic saline in the treatment of severe brain injuries, J. Neurosurg. 114 (2011) 545–548, https://doi.org/10.3171/2010.5.JNS091685.

[52] K. Järvelä, M. Koskinen, T. Kööbi, Effects of hypertonic saline (7.5%) on extracellular fluid volumes in healthy volunteers, Anaesthesia. 58 (2003) 878–881, https://doi.org/10.1046/j.1365-2044.2003.03332.x.

[53] J. Spadavecchia, D. Movia, C. Moore, C.M. Maguire, H. Moustaoui, S. Casale, et al., Targeted polyethylene glycol gold nanoparticles for the treatment of pancreatic cancer: from synthesis to proof-of-concept in vitro studies, Int. J. Nanomedicine 11 (2016) 791–822, https://doi.org/10.2147/IJN.S97476.

[54] K.B. Johnsen, M. Bak, P.J. Kempen, F. Melander, A. Burkhart, M.S. Thomsen, et al., Antibody affinity and valency impact brain uptake of transferrin receptor-targeted gold nanoparticles, Theranostics. 8 (2018) 3416–3436, https://doi.org/10.7150/thno.25228.

[55] R. Vinhas, A.R. Fernandes, P.V. Baptista, Gold nanoparticles for BCR-ABL1 gene silencing: improving tyrosine kinase inhibitor efficacy in chronic myeloid Leukemia, Mol Ther Nucleic Acids. 7 (2017) 408–416, https://doi.org/10.1016/j.omtn.2017.05.003.

[56] J.L. Markman, A. Rekechenetskiy, E. Holler, J.Y. Ljubimova, Nanomedicine therapeutic approaches to overcome cancer drug resistance, Adv. Drug Deliv. Rev. 65 (2013) 1866–1879, https://doi.org/10.1016/j.addr.2013.09.019.

[57] W.A. Banks, From blood-brain barrier to blood-brain interface: new opportunities for CNS drug delivery, Nat. Rev. Drug Discov. 15 (2016) 275–292, https://doi.org/10.1038/nrd.2015.21.

[58] G.C. Terstappen, A.H. Meyer, R.D. Bell, W. Zhang, Strategies for delivering therapeutics across the blood-brain barrier, Nat. Rev. Drug Discov. 20 (2021) 362–383, https://doi.org/10.1038/s41573-021-00139-y.

[59] B.M. Bruel, A.W. Burton, Intrathecal therapy for cancer-related pain, Pain Med. 17 (2016) 2404–2421, https://doi.org/10.1093/pm/pnw060.

[60] K. Ng, V.H. Mabasa, I. Chow, M.H.H. Ensom, Systematic review of efficacy, pharmacokinetics, and administration of intraventricular vancomycin in adults, Neurocrit. Care. 20 (2014) 158–171, https://doi.org/10.1007/s12028-012-9784-z.

[61] A. Ruggiero, V. Conter, M. Milani, E. Biagi, I. Lazzareschi, P. Sparano, et al., Intrathecal chemotherapy with antineoplastic agents in children, Paediatr Drugs. 3 (2001) 237–246, https://doi.org/10.2165/00128072-200103040-00001.

[62] V. Moen, N. Dahlgren, L. Irestedt, Severe neurological complications after central neuraxial blockades in Sweden 1990-1999, Anesthesiology. 101 (2004) 950–959, https://doi.org/10.1097/00000542-200410000-00021.

[63] M. Khani, G.K.R. Burla, L.R. Sass, O.N. Arters, T. Xing, H. Wu, et al., Human in silico trials for parametric computational fluid dynamics investigation of cerebrospinal fluid drug delivery: impact of injection location, injection protocol, and physiology, Fluids Barriers CNS. 19 (2022) 8–16, https://doi.org/10.1186/s12987-022-00304-4.

[64] M.-C. Senut, Y. Zhang, F. Liu, A. Sen, D.M. Ruden, G. Mao, Size-dependent toxicity of gold nanoparticles on human embryonic stem cells and their neural derivatives, Small. 12 (2016) 631–646, https://doi.org/10.1002/smll.201502346.